

1 Deep mass redistribution prior to the Mw 8.8 Maule 2 Earthquake (Chile) revealed by GRACE satellite grav- 3 ity

4 Marie Bouih (1), Isabelle Panet (1,2), Dominique Remy (3), Laurent Longuevergne (4),
5 Sylvain Bonvalot (3)

6

7 (1) Université de Paris, Institut de physique du globe de Paris, CNRS, IGN, F-75005 Paris,
8 France

9 (2) ENSG-Géomatique, IGN, F-77455 Marne-la-Vallée, France

10 (3) GET, Université de Toulouse, IRD, UMR 5563 CNRS, CNES, Toulouse, France

11 (4) Univ Rennes, CNRS, Geosciences Rennes - UMR 6118, F-35000 Rennes, France

12

13 Corresponding author: Marie Bouih (bouih@ipgp.fr)

14 Abstract

15 Subduction zones megathrust faults constitute a considerable hazard as they produce most
16 of the world's largest earthquakes. However, the role in megathrust earthquake genera-
17 tion exerted by deeper subduction processes remains poorly understood. Here, we analyze
18 the 2003 – 2014 space-time variations of the Earth's gravity gradients derived from three
19 datasets of GRACE geoid models over a large region surrounding the rupture zone of
20 the Mw 8.8 2010 Maule earthquake. In all these datasets, our analysis reveals a large-
21 amplitude gravity gradient signal, progressively increasing in the three months before the
22 earthquake, North of the epicentral area. We show that such signals **are equivalent to a**
23 **60 km³ water storage decrease over 2 months and** cannot be explained by hydrological
24 sources nor artefacts, but rather find origin from mass redistributions within the solid
25 Earth on the continental side of the subduction zone. These gravity gradient variations

26 could be explained by an extensional deformation of the slab around 150-km depth along
27 the Nazca Plate subduction direction, associated with large-scale fluid release. Further-
28 more, the lateral migration of the gravity signal towards the surface from a low coupling
29 segment around -32.5° North to the high coupling one in the South suggests that the
30 Mw 8.8 Maule earthquake may have originated from the propagation up to the trench of
31 this deeper slab deformation. Our results highlight the importance of observations of the
32 Earth's time-varying gravity field from satellites in order to probe slow mass redistributions
33 in-depth major plate boundaries and provide new information on dynamic processes in the
34 subduction system, essential to better understand the seismic cycle as a whole.

35

36 **Keywords**

37 Gravity gradients, GRACE, Earthquake, **Signal separation**

1 Introduction

The February 27th, 2010, M_w 8.8 Maule earthquake is one of the largest **instrumental earthquakes instrumentally recorded earthquakes**. It nucleated in the central region of the historic 1835 Concepcion event (M_w 8.5), matching a zone of high coupling previously characterized as a mature seismic gap [41]. This event ruptured a 500-km length segment of the interface between the downgoing Nazca and the over-riding South American plates, releasing stresses accumulated over more than 175 years since the last M_w 9 earthquakes in 1730 and 1751 [48]. It produced up to 7-12 meters of thrust slip in the 24-35km depth range. The largest slip (~ 16 m) was found in the northern portion of the ruptured zone, where a M_w 7.7 earthquake occurred in 1928 [22] [33].

The slip distribution of the 2010 Maule earthquake has been derived from seismological records [22], tsunami data and space geodetic observations [27][11]. While the seismological data are sensitive to the propagation of the rupture during the event, space geodesy detects the surface motions offsets after the rupture and their slow post-seismic variations, continuously over years or decades in the case of the **GNSS Global Navigation Satellite Systems (GNSS)**. Based on these two types of observations, the earthquake slip distribution is however not fully constrained at depth (e.g. [25]) and the post-seismic deformation processes remain debated, from localized afterslip in the seismogenic zone to viscous flow in the mantle. Ambiguities result in particular from a limited spatial distribution of the ground stations, mostly on land, and an imperfect knowledge of material properties of the Earth.

At medium spatial scales, co-seismic and post-seismic mass redistributions have been detected by the Gravity Recovery and Climate Experiment (GRACE) satellites. This mission measured the space-time variations of the Earth's gravity field with a decadal to monthly temporal resolution and 250-400km spatial resolution from 2002 to 2017 [47]. As for other giant ruptures monitored by GRACE, a co-seismic dipole marked by a predomi-

66 nant gravity decrease on the continental side of the subduction was observed for the Mw 8.8
67 Maule earthquake [17] [15] [9]. It was followed by ~~shorter and long-term post-seismic~~ **long-**
68 **and short-term post-seismic** signals featuring a slow gravity increase around the trench
69 [46] [8]. The homogeneous spatial coverage of satellite gravity provided key additional
70 information in order to constrain the geometric parameters of the ruptured fault and its
71 average slip [49] [9] and to discuss the nature of the post-seismic processes [46] [15].

72

73 Recently, regional-scale gravity variations have been detected in the GRACE geoids in
74 the months before the giant rupture of the March 2011 Mw 9.1 Tohoku-Oki earthquake.
75 They have been attributed to slab deformation at mid-upper mantle depth, eventually lead-
76 ing to the seismic slip as the deeper motion propagated towards the surface [36]. These
77 results have been corroborated by independent GNSS data exhibiting regional crustal de-
78 formations of a few millimeters from October 2010 to March 2011, which have been related
79 to slab extension prior to the earthquake, near 50-100km depth [2]. Thus, geodesy and
80 gravity open new ways to analyze the subduction process from depth to surface, including
81 the occurrence of giant ruptures. The unique sensitivity of satellite gravity to deeper mass
82 redistributions offered an information complementary to the surface displacements in order
83 to monitor aseismic motions at all depths in the subduction system.

84

85 Deciphering these tenuous solid Earth signals in the gravity field variations however
86 requires to resolve a separation challenge: the GRACE data integrate the total gravity
87 change induced by all the mass variations within the near-surface fluid layer and the solid
88 Earth. We need to decipher the signals from different sources such as hydrological, atmo-
89 spheric and oceanic mass variability or viscoelastic Earth deformation from post-glacial
90 rebound [4] [35], predominant in the total gravity signal. This is a major challenge in
91 the application of satellite gravity data to track deeper deformations, calling for dedicated
92 analysis techniques. To solve this separation challenge, we will analyze horizontal gravity
93 gradients rather than the geoid. Indeed, gravity gradients help identify a source from the
94 spatial shape of its gravity signal, which is finely described thanks to the double differ-

95 entiation of the gravity potential [36]. This way we can unravel smaller signals if their
96 geometry differs from that of the predominant ones.

97

98 Here, we investigate whether anomalous gravity variations preceding the 2010 Maule
99 event can be detected in the GRACE data. We consider a broad space-time window around
100 the earthquake, from January 2003 to July 2014 in a $90^\circ \times 120^\circ$ wide region around Central
101 Chile. We first analyze different sets of GRACE gravity field models to search for abnormal
102 signals before the rupture. For that, we enhance small gravity variations using gravita-
103 tional gradients reconstructed from GRACE at different spatial scales. Then, we evaluate
104 the obtained signals with respect to independent estimations of water storage changes by
105 hydrological models and in-situ observations. This analysis allows us to propose and dis-
106 cuss a deeper origin inside the solid Earth, involving slab deformations near 150-km depth
107 prior to the rupture.

108

109 2 Data and methods

110 2.1 GRACE geoid models

111 To search for gravity signals associated ~~to~~ with the Maule earthquake in the South Amer-
112 ican subduction system, we apply a space-time analysis of the time series of the GRACE
113 geoid models over the January 2003-September 2014 period. To assess the sensitivity of
114 the signals to the North-South oriented striping noise that degrades the GRACE geoids, we
115 considered three sets of geoid models obtained by different groups, provided in the form of
116 spherical harmonics expansions: the CNES/GRGS Release 3v1 (GRGS) up to degree/order
117 80 [24], ~~the ITSG-2016 solution up to degree/order 90 60 [30] and the CSR Release-06~~
118 ~~solution (CSR) up to degree/order 90 60 [42]~~ the CSR Release-06 solution (CSR) up to
119 degree/order 60 [42] and the ITSG-2016 solution up to degree/order 60 [30]. For the stud-
120 ied area at the beginning of 2010, we indeed found less striping in the North-South gravity

121 gradients in the ITSG-2016 solution as compared to the ~~more recent~~ ITSG-2018 release.
122 Due to a different analysis of the GRACE observations, the ITSG-2016 and CSR gravity
123 models show a higher level of striping artefacts than the GRGS solution. To minimize
124 ~~the striping~~ these artefacts in these last two fields, we truncated their spherical harmonics
125 expansion at the degree and order 40. We have verified that at this 500-km resolution, the
126 signal-to-noise ratio remains favourable.

127 2.2 Hydrological models and in-situ data

128 Separation of solid Earth and hydrological signals is based on both a model-driven and a
129 data-driven approaches. We considered an ensemble of four complementary hydrological
130 models: 1. GLDAS NOAH 2.1 land surface model [39], 2. WGHM global hydrological
131 model [34], 3. ERA5-Land land surface model [10] and 4. the regional MGB model for
132 South America [44]. For comparison with the GRACE observations, we reconstructed each
133 month the geoid and the gravity gradients predicted by these different models, considering
134 the direct newtonian attraction of the water loads and applying a thin layer approximation.
135 In specific regions, we estimate water storage changes from in-situ observations: river dis-
136 charge (Q) provided by the Global Runoff Data Centre (GRDC), precipitation (P) from the
137 Global Precipitation Climatology Center (GPCC) [43] and actual evapotranspiration (E)
138 provided by the Max Planck Institute [21] (see Appendix E for a more detailed description
139 of the used datasets).

140 ~~To separate solid Earth and hydrological signals, we designed both a model-driven~~
141 ~~and a data-driven approach to define the impact of water redistribution on gravity. We~~
142 ~~considered four complementary hydrological models: 1. The global GLDAS NOAH 2.1~~
143 ~~model (including soil moisture, snow and water stored in the canopy) at 0.25° resolution~~
144 ~~[39], 2. the global WGHM model (including soil moisture, snow, groundwater and surface~~
145 ~~water) at 0.5° resolution [34], 3. the global ERA5-Land model at 9-km resolution (including~~
146 ~~soil moisture and snow) [10] and 4. the regional MGB model for South America (including~~
147 ~~canopy, soil moisture, ground water and surface water) at 10-km resolution [44]. We~~

148 reconstructed each month the geoid and the gravity gradients predicted by these different
149 models, considering the direct newtonian attraction of the water loads and applying a thin
150 layer approximation. Here, the model ensemble is used to better quantify errors arising
151 from forcing data, model structure, and model spatial resolution.

152

153 In specific regions, we complete the model analysis with water storage changes inferred
154 from in-situ observations. We considered observations of river discharge (Q), precipitation
155 (P) and actual evapotranspiration (E). The precipitation is based on the Global Precipitation
156 Climatology Center (GPCC) “Full Data Monthly Version 2020” dataset [43]. The GPCC
157 provides gridded gauge-analysis products derived from quality controlled station data,
158 at 0.25° resolution [40]. The actual evapotranspiration is provided by the Max Planck
159 Institute [21]. It is estimated from a data-driven approach, based on a global monitoring
160 network, meteorological and remote-sensing observations, and a machine-learning algorithm.
161 Finally, we used river discharge data and basin outlines provided by the Global Runoff Data
162 Centre (GRDC). The hydrological analysis is performed over 2005-2012 when discharge
163 data is available, in order to remove properly annual and semi-annual signals. Furthermore,
164 in order to remove the potential impact of systematic bias in the fluxes data (e.g. [26]), a
165 linear trend is fitted on water storage changes over the 2005-2012 period.

166

167 2.3 Gravity gradients at different spatial scales

168 In order To separate signals associated with **from** mass sources of different sizes, shapes
169 or orientations in the GRACE geoids, we reconstruct each month from these geoid mod-
170 els the Earth’s gravity gradients at different spatial scales, expressed in spherical frames:
171 1) the distinction between signals of different sizes is made by a wavelet analysis of the
172 GRACE gravity potential [18]; 2) the source geometry is emphasized by computing **hor-**
173 **izontal** gravity gradients. In cartesian coordinates, these **gravity** gradients result from a
174 double differentiation of the wavelet-filtered gravity potential with respect to the three

175 directions of space [35]; then they are expressed at each point in the local spherical frame
176 through appropriate coordinate transformations. As they highlight gravity signals **elon-**
177 **gated** orthogonal to the differentiation direction, the ~~obtained~~ **horizontal** gradients provide
178 us with a detailed description of the geometry of the gravity field variations at each spatial
179 scale, reflecting the structure and spatial extent of the sources (Appendix Fig. S1). From
180 a general point of view, rotating the spherical frame along the radial axis is well-suited to
181 separate gravity variations along the orientation of a subduction zone which could be po-
182 tentially related to an earthquake, from water mass redistribution signals following other
183 orientations. As both GRACE noise and the South-American subduction zone follow a
184 North-South orientation, we average the gradients over a range of orientation ($\phi\phi$ gravity
185 gradients from -10 to 10° clockwise spherical frame rotations) around the North-South
186 direction to increase signal-to-noise ratio, and we used directions close to East-West, or-
187 thogonal to the GRACE noise. The same methodology is applied to hydrological models.

188 **2.4 Piece-wise linear fit of anomalous signals**

189 We then analyze the time series of gravity gradients at the different scales and in the dif-
190 ferent orientations, in order to search for anomalously large gravity variations before the
191 Maule earthquake and compare them with the consecutive co-seismic signals. We first esti-
192 mate and remove from the time series annual and semi-annual sinusoidal terms accounting
193 for the seasonal variability and a long-term trend, all estimated over the 2003/01-2008/12
194 period to limit the potential impact of a precursor, and apply the correction to the whole
195 time series. Then, we analyze the residual time series $g(t)$ as follows:

196

- 197 • We perform a piece-wise linear fit [36] of the time series $g(t)$ with a free jump in March
198 2010, which is the first month actually recording the co-seismic step in the GRACE data
199 (Appendix Fig. S2). For that, we decompose the time series of gravity gradients into four
200 consecutive segments separated by a free step in March 2010: [January 2003 - t_1], [t_1 -
201 February 2010], [March 2010 - t_2] and [t_2 - September 2014] with $t_1 =$ July 2009 and $t_2 =$

202 March 2011. The first interval is the reference before the earthquake. The second interval
203 represents the variations in the months preceding the earthquake, potentially including a
204 fast pre-seismic signal. It is fixed to 8 months as a compromise between a too short interval
205 (for which the trend estimate would be very sensitive to noise) and a too long one (for
206 which the meaning of a sudden pre-seismic gravity variation would be lost). **Actually, our**
207 **conclusions do not change when we vary the length of this interval between 1 and 8 months.**
208 The free jump in March 2010 highlights the co-seismic signal. For the two last intervals,
209 we take t_2 equal to March 2011. This way, we account for variations of the post-seismic
210 gravity signals between the first year and the rest of the time series.

211

212 • Anomalous variations before the earthquake are identified by the combination of 1. a
213 large trend (>0.1 mEötvös) over the 8 months interval preceding the rupture in the piece-
214 wise linear fit, together with 2. an abnormal gravity gradient signal in the month before
215 the earthquake (February 2010), marked by a very low probability of occurrence in the ob-
216 servations ($\geq 5\sigma$, i.e. probability below $2.5 \cdot 10^{-6}\%$). To detect these abnormal variations
217 in the monthly gravity gradients, we assume that the time series of residuals $g(t)$ follow a
218 Gaussian distribution and calculate its parameters, at each spatial grid point, over the ref-
219 erence period 2003/01-2008/12. This way we detect anomalous signals before the rupture,
220 both in the February 2010 monthly snapshot and at a timescale of a few months, without
221 making any hypothesis on the behaviour of the rest of the time series after February 2010
222 (such as the occurrence of a co-seismic variation). This approach allows us to detect a large
223 and monotonous variation progressively realized over a few months, which culminates in
224 highly abnormal values at the end of the considered period.

225

226 • We search for the co-seismic signal, identified by the combination of 1. a large jump
227 in March 2010 in the piece-wise linear fit, together with 2. an abnormal gravity gradient
228 signal in March 2010 (probability below $2.5 \cdot 10^{-6} \%$), and 3. a shift in the distribution of
229 the residual time series $g(t)$ after the earthquake as compared to the years before, indi-
230 cating some degree of persistence over time of the co-seismic jump (“step-like” temporal

231 variation). This last criterium is simply implemented by a threshold in the amplitude of a
232 Heaviside function centered at the time of the earthquake.

233

234 This method enables us to make a clear distinction between fast variations right before the
235 rupture and the co-seismic variation itself. The co-seismic amplitude is given by the jump
236 in the piece-wise linear fit, while the linear trends after the rupture can approximate faster
237 and slower post-seismic signals. ~~Over these relatively short post-seismic time intervals,~~
238 ~~exponential and logarithmic behaviors, as may be expected in the presence of afterslip or~~
239 ~~visco-elastic deformations, can be approximated by linear evolution [19].~~ Fitting the post-
240 seismic behavior is required to better estimate the pre- and co-seismic signals but remains
241 beyond the scope of the paper.

242 3 Results

243 3.1 Slow to fast gravity jumps near the epicenter

244 We present here the results obtained for an analysis scale of 800-km, commensurate with
245 the rupture length. At larger spatial scales, the earthquake signals progressively decay as
246 the scales become too large as compared to the spatial extent of the signal. The smallest
247 spatial scale that can be reached (500-km) given the resolution of the GRACE geoids is
248 presented in the Section 4.2.1.

249

250 Around the epicenter, the two-lobe gravity signal confirms the impact of the co-seismic
251 jump during the month of March 2010 (Fig. 1b, zoomed in Fig. 1d) that was observed
252 in previous studies. It comprises a negative gravity gradient anomaly over the ocean and
253 a positive one over the continent with amplitudes up to 0.19 mEötvös, persistent in the
254 consecutive years. For comparison, the co-seismic gravity gradient signature of the 2011
255 Tohoku earthquake is twice larger at this spatial scale. Furthermore, we find that this
256 co-seismic variation is preceded by an anomalously large gravity gradient increase in the

257 months before the rupture, located North of the epicentral area (Fig. 1a, zoomed in Fig.
258 1e)(Fig. 1a,c). It stands out as the most abnormal signal over the entire South American
259 continent, manifested by the most widespread February 2010 anomaly. This signal exceeds
260 the 5σ level of the long-term distribution, after a large increase over 8 months. Thus,
261 among all the medium-scale gravity variations in the months before the earthquake, the
262 largest one is the closest to the epicenter. It is also detected in the wavelet-filtered geoid,
263 although less well separated from neighbouring hydrological sources (Appendix B).

264

265 These variations are reflected in time series of the gravity gradients at different locations
266 within these signals (Fig. 1e). For points near the maximum of the co-seismic anomaly
267 below the latitude -34°N , a large and sudden jump is observed between February and
268 March 2010, starting from a high value in the time series in February. As we move towards
269 the North (above latitude -34°N), away from the epicenter, the co-seismic jump decreases
270 while an anomalously large positive trend is observed in the preceding months, leading to
271 a slow jump in the time-series. Because of this gradual increase, ending up with two highly
272 anomalous values in January and February 2010, we infer a duration of the signal of at
273 least 2 months. At the monthly resolution of the used GRACE data, and in the presence of
274 hydrological contributions, it remains difficult to point out the exact starting time of this
275 signal, which might be earlier in 2009, and whether it develops continuously or through
276 pulses at submonthly timescales.

277

278 We have assessed the sensitivity of the February 2010 GRACE monthly geoid to the co-
279 seismic mass redistributions. The Maule earthquake took place at 6 : 30 UTC on February
280 27, 2010. When counting the number of February 2010 orbits in a 20° vicinity of the
281 epicenter, we find less than 5% of the monthly orbits in the time interval after the rupture.
282 This confirms that the February 2010 signal North of the epicenter is not significantly
283 impacted by the co-seismic signal, and that the latter which is first recorded in the March
284 2010 geoid.

285 3.2 Singularity of the gravity gradient signal before the rupture

286 We have investigated the unique character in space and time of the gravity gradient increase
287 before the earthquake. The spatial unicity over the South American continent is illustrated
288 from Fig. 1a, where the signal near Maule appears as the largest one. The unicity of
289 this signal in time can be directly observed from the time series in Fig. 1e. These time
290 series show that, in the considered region near the Maule 2010 epicentral area, a signal
291 of a comparable amplitude had not been recorded before, nor in the consecutive years
292 (note that the annual cycle correction may degrade in the end of the time series). This is
293 confirmed when repeating the same time series analysis as described above, for hypothetic
294 earthquake times t_e spanning the [March 2004 - March 2010] interval with a monthly time
295 step. Appendix Fig. S4 shows the obtained anomalous signals cumulated over the [t_e
296 - 9 months to t_e - 1 month] intervals: there is no equivalent to the July 2009 - February
297 2010 gravity gradient signal over the whole period and the whole continent.

298 3.3 Investigation of other GRACE gravity solutions

299 To assess the robustness of the signals before the rupture, we tested whether they could
300 also be found in two other sets of GRACE geoid models, the CSR06 and the ITSG-2016
301 solutions, in addition to the GRGS solution. For that, we extracted their common space-
302 time patterns of variability using a Singular Value Decomposition between pairs of models
303 (expressed in terms of gravity gradients): 1. GRGS03 versus CSR06 and 2. GRGS03 ver-
304 sus ITSG-2016. We found a highly coupled behaviour of each pair of solutions, featuring
305 a slow jump initiated a few months before the earthquake in the region of the pre- and
306 co-seismic signals, in both the North-South and the East-West directions (Appendix Fig.
307 D.2) (Appendix D.2, Appendix Fig. S5). As each individual solution, the average of these
308 three datasets shows the same behaviour (Fig. 2a-d). It is illustrated by the following
309 analysis allowing us to identify a slow jump near March 2010 completed to a large extent
310 in February 2010. As the CSR and ITSG-2016 solutions show more a higher level of strip-
311 ing noise than the GRGS one, we use a more constrained time evolution model, with less

312 degrees of freedom than done for GRGS in the previous section. For that, in each set of
313 GRACE solution ~~as well as~~ **and** in their average, we estimated a Heaviside step function in
314 March 2010. This estimate is not very sensitive to the exact timing of the step, due to the
315 length of the time series: it will not distinguish between steps completed in February or in
316 March. We define anomalous signals in February 2010 such that their amplitude exceeds
317 50 % of the estimated step, and their probability of occurrence is low (assuming a Gaussian
318 distribution of the monthly gravity gradient values, as done before).

319

320 Figure 2 presents the results obtained for each of the three gravity gradient solu-
321 tions ~~used in this study for one direction (North-South)~~ **(in the North-South direction)**
322 and for their average ~~for two ranges of orientations (North-South and East-West)~~ **(in the**
323 **North-South and East-West orientations)**. A good agreement is found between the three
324 solutions: the North-South oriented gravity gradient exhibits an anomalous increase be-
325 fore the earthquake in the same area for each individual solution and their average (Fig.
326 2a-d). The ~~above discussed~~ temporal pattern of a slow jump in the gravity gradients is
327 detected in both North-South and East-West directions (Fig. 2f-g). It is associated with
328 a well-resolved spatial pattern in the same area for both orientations, pointing to anoma-
329 lously large signals during that month (Fig. 2d-e). This behaviour appears unique over
330 all South America (Fig. 2a-c). ~~Finally, we have also~~ **We finally** investigated anomalously
331 large signals in February 2010 without any constraint on a step-like evolution of the time
332 series. A few other signals are detected in the CSR and ITSG-2016 solutions, in addition to
333 the gravity gradient increase before the Maule earthquake (Appendix Fig. S11). However,
334 the ~~singularity~~ **specificity** of the February 2010 signal in the region of Maule is further
335 evidenced from comparisons with hydrological models and in-situ data.

336 4 Sources of the gravity signal before the earthquake

337 4.1 Inaccuracies in the GRACE data processing

338 We have investigated whether the gravity signal before the Maule earthquake could result
339 from inaccuracies in the data analysis: (1) striping artefacts, (2) errors in the atmospheric
340 dealiasing model, or (3) over or under-correction of the seasonal cycle. First, we estimated
341 empirically the level of striping errors in the monthly horizontal gravity gradients from
342 2003 to 2014, for the 500-1000km spatial scales. For that, we computed each month the
343 rms of the gravity gradients over a wide oceanic area centered at the latitude of the Maule
344 earthquake epicenter. We conclude that the February 2010 anomalous gravity gradient
345 variations exceed the noise by a factor 4 to 8 depending on the spatial scale. Looking
346 then at the atmospheric dealiasing model of the GRGS geoids, based on the ECMWF
347 ERA-Interim reanalysis [10], we find that, in the region of Maule, the amplitude of the
348 February 2010 non-seasonal atmospheric signal is hundred times smaller than the GRACE-
349 observed anomaly before the rupture. This reflects the fact that the modelled atmospheric
350 contribution is almost purely seasonal in the studied area. We finally investigated whether
351 the gravity signal before the earthquake could result from an over- or under-correction of
352 the seasonal cycle in the GRACE data or in the atmospheric model. We first remark that
353 an error in a periodic correction should appear as a periodic residual in the time series. Such
354 behaviour is absent from the gravity gradient time series shown in Fig. 1e until 2011 at
355 least. Comparing the amplitude of the GRACE pre-seismic signal with that of the seasonal
356 cycles fitted in the GRACE data or in the modelled atmospheric contribution at the ~~same~~
357 ~~location (north of the epicenter)~~ **north of the epicenter**, we notice that the February 2010
358 ~~anomalous GRACE~~ gravity gradient signal is at least two times larger than the amplitude
359 of the GRACE seasonal cycle and ten times larger than that of the atmospheric model
360 ~~there~~. Thus, neither the striping artefacts nor the atmospheric or seasonal corrections can
361 explain the observed variations.

4.2 Hydrological signals from global and regional models

4.2.1 Predicted signals in the vicinity of the epicentral area

Most of the gravity signal recorded by GRACE comes from continental water mass redistribution, so we investigated a possible hydrological source to the gravity gradient increase before the earthquake. **Note that the GIA gravity gradient signal from the Patagonian Ice Field does not affect our results due to different timescale, and even more so as we have removed a long-term trend from the data.** The horizontal gravity gradients increase corresponds to mass decrease, hence a drying signal. We first compare the GRACE anomaly with the predictions of the hydrological models presented in the Section 2.2.

In addition to the scale 800-km, we present here the results at the 500-km scale. As shown in Fig. 3, this 500-km scale gives access to finer details including large hydrological signals that might be not resolved at the 800-km scale (Fig. 3c,e). This higher resolution is ~~interesting because it~~ provides a better spatial separation between sources in the Andean Cordillera and those in the watersheds of Argentina, especially the major La Plata basin (hydrological context map Appendix Fig. S7). This smaller spatial scale is closer to the characteristic scale of some drainage basins in the region than the scale 800-km ; at the same time it brings other challenges as we notice a higher number of anomalous signals in the GRACE gravity gradients. They include a large negative anomaly in the La Plata basin (labelled 3 in Fig. 3c), and a positive anomaly around the point (294.5°E ; -31°N), labelled 2 in Fig. 3c. This positive signal is located at the North-East of the 800-km scale GRACE anomaly before the earthquake, which integrates the 500-km scale anomalies 1 and 2 (Fig. 3e).

We first compare the time evolution of the GRACE-observed signal with that predicted from the hydrological models at locations spanning the corresponding area. Fig. 3a shows that GRACE and the models are coherent in the North-Eastern lobe (anomaly 2). In the southern lobe closer to the epicenter (anomaly 1, especially between latitudes -33°N

390 and -34.5°N), GRACE and the models agree from 2004 to the end of 2009 but this
391 consistency degrades starting from January 2010, after five years of low variability. At
392 the beginning of 2010, the GRACE time series indeed exhibit a fast and large increase
393 whereas the hydrological signals remain in the continuity of the previous years. Thus, the
394 North-Eastern component of the GRACE signal (anomaly 2) is probably impacted by a
395 hydrological contribution near the western end of the Plata basin, a temperate climate area
396 (Fig. 3d, Appendix Fig. S8), while the South-Eastern component of the signal (anomaly
397 1) remains anomalous with respect to the hydrological models. Interestingly, it is located
398 in an arid zone, as discussed later in this work.

399 **4.2.2 Spatial patterns of the modelled hydrological signals**

400 These differences are confirmed when investigating the localization of the hydrological
401 signals. Because the GRACE signal is probably not related to a variation in the seasonal
402 cycle, we investigate the spatial patterns of the residual non-seasonal variability. During
403 the 6 months period before March 2010 (September 2009 - February 2010) as well as in the
404 7 years before, the GLDAS, WGHM and MGB models do not predict any non-seasonal
405 500-km scale signal in the region of the GRACE anomaly 1, in both North-South and East-
406 West directions (Appendix Fig. S8, S9). The hydrological signals are indeed controlled
407 by the topographic reliefs of the Andes and the Chilean Coast Range, which localizes the
408 rainfalls in a thin North-South elongated band on the Western flank of the mountains in
409 Southern Chile, mostly south of the considered area. In contrast, the GRACE anomaly
410 2 is likely affected by a non-seasonal hydrological contribution from the western part of
411 the La Plata basin. When comparing the hydrological models, we found a disagreement
412 of ERA5-Land with the other models. This is mostly due to differences in the seasonal
413 cycle predicted by this model, leading to residual annual signals in the region of Maule
414 (Appendix Fig. S10), unobserved by GRACE.

4.2.3 Comparison of different hydrological basins

In a last comparison, we estimated the GRACE anomalous signals in February 2010 in all the investigated gravity field solutions (GRGS, CSR and ITSG-2016) **the GRGS, CSR and ITSG gravity field solutions** without any hypothesis on a step-like evolution of the time series in March 2010. With a lower level of abnormality of the February 2010 signal than in Fig. 1, we detect anomalous gravity gradient variations also over the Orenoco, Chaco and La Plata basins (Appendix Fig. S7, S11). These anomalous ~~gravity gradient~~ variations are probably related to the 2009-2010 El Niño event, which resulted in large mass redistributions associated with droughts in the Amazon basin and floods in the La Plata basin. We notice that the GRACE signals agree well with the predictions of the hydrological models in all the drainage basins, except for the anomaly located north of the epicenter of the Maule earthquake (Appendix Fig. S11). There, El Niño brings increased precipitations in winter (from June to December), and has no direct impact on the summer rainfalls [7]. Thus, it seems hardly consistent with the GRACE mass variations in this area, contrary to the other basins.

4.3 In situ observations

As a complement to the hydrological models, we investigated in-situ observations of horizontal and vertical water fluxes (river discharges, precipitations and evapo-transpiration).

The GRACE signal is located in the region of Mendoza in Argentina, considered arid with its 150 to 300 mm of annual rainfall (Fig. 4a), and part of the so-called Arid Diagonal of South America. Most of the water in the watersheds comes from the annual melting of snow and ice and is transported from the mountain by the rivers ; it is collected through artificial dams by the regional population, ~~organized in three oases~~. Therefore, the rivers discharge upstream of the dams is representative of the water influx in the zone and appears significantly correlated with the regional snow accumulation at inter-annual timescales [29]. Fig. 4b-f shows the variations of discharge at five stations upstream of the dams in the

442 Central Andes over the 2000-2017 period. First, we notice that the annual discharge shows
443 a large decrease starting at the end of 2010. This decrease coincides with the beginning
444 of a mega-drought in Central Chile, manifested as a sequence of dry years with reduced
445 annual precipitations [14]. However, Fig. 4 also shows that the effect of this mega-drought
446 on the river flows is still limited in February 2010; it starts later that year, together with a
447 strong 2010/2011 La Nina episode initiated in June [14]. Thus, this mega-drought cannot
448 explain the GRACE mass decrease signal observed five months before, in February 2010.

449

450 Second, we compared the mass anomaly explaining the GRACE signal before the earth-
451 quake with the water storage variation corresponding to these discharge data. Here we
452 neglect the impact of the vertical water fluxes, which is consistent with an influx of water
453 mostly from snow and ice melting in this region. The 0.18 mEötvös (resp. 0.19 mEötvös)
454 amplitude of the GRACE signal at the 800-km scale (resp. 500-km scale) can be mod-
455 elled by a water mass source of width 4500-km, length 500-km and thickness 300 mm
456 EWH (Equivalent Water Height). It corresponds to $\sim 60 \text{ km}^3$ of water storage decrease
457 between the beginning of January 2010 and the end of February 2010, or a discharge of
458 $30 \text{ km}^3 \cdot \text{month}^{-1}$ during two months. Distributing this mass transport over the four ma-
459 jor rivers of the region (Mendoza, Desaguadero, Tunuyan and San Juan) still leads to a
460 $7.5 \text{ km}^3 \cdot \text{month}^{-1}$ flow. This is fifteen times more than the largest monthly flow recorded
461 in the region for the period 2000-2017 ($0.5 \text{ km}^3 \cdot \text{month}^{-1}$ for the Mendoza river in 2006,
462 Fig. 4c), and still much larger than the maximum historical discharge of $1 \text{ km}^3 \cdot \text{month}^{-1}$,
463 recorded in 1987 [32].

464

465 To complete our analysis of the hydrological sources in this region, we carried out a more
466 precise estimation of the water storage variations of the four watersheds intersecting the
467 GRACE anomaly, for comparison with the GRACE-observed mass transport in February
468 2010. For that, we estimate the water storage change (S-S0) at basin scale from in-situ
469 observations of fluxes, namely precipitation grids (P), actual evapotranspiration (E) grids
470 and river specific discharge (Q). These variables are related via the mass balance equation

471 $\frac{dS}{dt} = P - E - Q$, which is integrated to derive storage variations per unit surface $S - S_0 =$
472 $\int \Delta S dt$, in mm EWH in each basin, which is transformed in volume in km^3 by multiplying
473 by the basin area. In the above equation, the river discharge (Q) defines the basin response
474 to the effective rainfall ($P-E$). Here, the river discharge stations are located downstream
475 of each basin on which we apply the mass balance equation. As shown in Fig. 5, the
476 obtained water storage variations amount to $\sim 1.2 \text{ km}^3$ over two months between January
477 and February 2010. This value is far smaller than the dozen of km^3 of water needed to
478 explain the GRACE signal. Thus, the observed gravity gradient anomaly is not likely to
479 be explained by a water source in this regional context.

480 5 Implications for deep Earth pre-seismic processes

481 The above analysis supports a solid Earth origin of this gravity gradient signal, involving
482 mass decrease at depth. Here, we discuss its possible origin in the context of the South
483 American subduction.

484

485 Multiple lines of evidence indicate that a regional change in stress state inside the crust
486 along the South Chile subduction zone occurred prior to the megathrust earthquake, in
487 relation with deeper slab motions. Bouchon et al [5] report a pre-earthquake seismic ac-
488 tivity which began in early January 2010. This activity was characterized by an initial
489 burst of seismic activity at depth followed by shallow foreshocks. In the USGS catalog, a
490 large (M_w 5.8) intermediate-depth earthquake (depth $\sim 150\text{-km}$) occurred on 12 February
491 2010 in the region where the pre-seismic gravimetric signal is reported, suggesting that the
492 change in stress state affected a very wide area around the epicenter region. Large-scale
493 anomalous GNSS displacements were detected four months before the main event over the
494 whole South Chile subduction zone, corroborating such a hypothesis [2]. The spatial and
495 temporal correlation between the shallow and the deep seismicity activities, the extensional
496 mechanism of the deep shocks and the trenchward motion of 4-8 millimeters lead the au-
497 thors of these previous studies to the same conclusion. Bouchon et al. [5] and Bedford

498 et al. [2] propose that these observations are related to a sudden increase of slab pull at
499 depth interacting with shallow slow slip further updip.

500

501 All these observations support an extensional deformation of the slab along its sub-
502 duction direction. Also observed in the case of the 2011 Tohoku-oki earthquake [36], such
503 deformation is consistent with our GRACE pre-seismic mass decrease signal. To evaluate
504 its magnitude, we modeled a pre-seismic intra-slab extension using a model of quasi-static
505 normal faulting in a vertically stratified elastic medium. We found that the observations
506 can be explained by 1.5 m of slip along a 45° dipping, North-South striking plane of width
507 100-km and length 500-km, located between the depths 115 and 185-km (Fig. 6). This
508 corresponds to a Mw 8.2 event over a few months. As in the case of the Tohoku-oki earth-
509 quake, where a precursor signal equivalent to a Mw 8.4 rupture was detected [36], the
510 magnitude of the pre-seismic event is smaller than that of the consecutive co-seismic rup-
511 ture and its spatial extent is commensurate with the length of the co-seismically ruptured
512 area. This corresponds to a smaller amount of deep deformation distributed over a wider
513 zone around 250-km depth before the Tohoku-oki 2011 earthquake, and a larger but more
514 localized deformation around 150-km depth before the 2010 Maule earthquake.

515

516 Interestingly, for both Maule and Tohoku, this pre-seismic gravity signal occurs in a
517 region where the geometry of the subduction changes. The Tohoku pre-seismic signal co-
518 incides with a change in the strike of the subduction, in the vicinity of a triple junction. In
519 the case of Maule, the gravity pattern before the rupture is located ~ 400 -km North-East
520 of the epicenter, in a transition section where the dip of the subducted Nazca plate changes
521 sharply. North of -33°N , the Nazca plate remains sub-horizontal at about 100-km depth
522 for several hundred kilometers, before dropping steeply into the mantle. South of -33°N ,
523 the slab plunges continuously at an angle of 25° [6] [38]. This change of dip is associated
524 with a slab hole at $\sim 200 - 300$ km depth, at the latitudes of the February 2010 GRACE
525 signal [28] [38]; mantle flow through this opening at depth in the flat slab is suggested
526 from seismic tomography. The rapid change of slab geometry causes an increase of the

527 slab stresses, due to localized lateral deformations[1]. In addition, mantle flow beneath the
528 flat slab and through the slab hole [28] [13] may contribute to entrain the motion of the
529 subducted plate towards the depth.

530

531 The spatial and temporal synchronization observed between the pre-seismic gravity
532 signal with the megathrust earthquake suggests that these two events are linked. We
533 thus propose that, between the end of 2009 and March 2010, the deep pre-seismic slab
534 deformation migrated both upwards to the surface and laterally along the slab. From
535 the pre-seismic to the co-seismic phase, the gravity gradient signal indeed shifts from the
536 North/East (around the point $292^{\circ}\text{E}; -32.5^{\circ}\text{N}$, corresponding to a 150-km depth for the
537 top of the slab) to the South/West (around the point $290^{\circ}\text{E}; -36^{\circ}\text{N}$). This lateral mi-
538 gration towards the surface is reminiscent of the variations of coupling of the subduction
539 interface, at the shallower depths. The pre-seismic extension is indeed located downdip a
540 transition area between a low coupling segment in the North and a high coupling one in the
541 South [31], and the motion propagates towards the more coupled zone in the South, where
542 the rupture occurred [31] in the historical seismic gap of central Chile [48]. Comparing our
543 co-seismic gravity gradient signal with that predicted from a geodesy-based co-seismic slip
544 distribution model [27], we found a reasonable agreement between the GRACE-derived
545 co-seismic anomaly and the modelled one (Appendix Fig. S12).

546

547 Finally, the existence of a gravity gradient signal without large surface displacements
548 had been noticed for both the pre- and co-seismic signals of the Tohoku-Oki earthquake,
549 and is again observed in the case of the Maule earthquake. In the Maule pre-seismic
550 phase, the slab deformation estimated above should have generated centimetric surface
551 displacements, which is one order of magnitude greater than the displacements highlighted
552 by Bedford et al.[2]. Even if the spatial coverage of the GNSS network is very sparse in
553 this region far of the trench, it is unlikely that such ground surface displacement remains
554 undetected. Considering other processes that may have contributed to the observed pre-
555 seismic gravity variation, we have investigated the effect of transient fluid release related

556 to oceanic plate dehydration. Upon subduction, hydrous minerals release water from the
557 slab over a range of depths [12] [37] [45] [20]; the mechanisms, dimensions and timescales
558 of fluid flow within the subduction zone are not well understood. Dehydration fluid is
559 generally considered as a continuous process occurring on a time scale of $10^5 - 10^6$ years
560 [12] [20]; however, it has been suggested that channelized fluid flows are highly localized,
561 accumulating and releasing high fluid volumes within short time interval (1-4 months) [20]
562 [37] [45]. The increasing slab pull force accommodated by extensional cracks and motion
563 along normal faults may have promoted the creation of fluid pathways, improving the
564 drainage of the subducting plate. Even if the mechanisms of large-scale fluid release from
565 the slab at depth remain unclear, a simple model based on a slight change of the porosity
566 ($10^{-5} - 10^{-6}$ of relative volume variation) of the slab segment in extension at depth is able
567 to fully or partially explain the the observed gravity gradient signal. We have modelled
568 the gravimetric signal caused by a fluid infiltration in the cracks generated by a deep
569 extension, i.e. a density variation of $\rho_{\text{fluids}} - \rho_{\text{rocks}} = -2400\text{kg.m}^3$ over a volume of width
570 200-km, length 500-km and thickness 80-km, with a porosity $\frac{\delta V}{V} = 5 \cdot 10^{-6}$, located around
571 150-km depth. According to this model, the fluid-related mass transfer at depth induced a
572 widespread gravity variation (Fig. 6e-f), able to explain the observed gravity gradient signal
573 (Fig. 6a-b). We thus hypothesize that the absence of large surface displacements could
574 be related to a significant contribution to the observed gravity signal of such deeper mass
575 redistributions associated with fluid migration, accompanying the extensional deformation
576 of the slab.

577 Conclusion

578 From a dedicated analysis of time series of GRACE-derived gravity gradients, we have
579 detected an anomalously large gravity gradient increase in the months before the Mw 8.8
580 2010 Maule earthquake, in the north of the epicentral area, most likely caused by mass
581 redistributions at depth within the solid Earth on the continental side of the subduction.
582 This gravity signal prior to the rupture can be explained by a deep extensional deformation
583 of the slab along the subduction direction, equivalent to a Mw 8.2 normal faulting event.
584 This event is commensurate with the precursor signal detected before the Tohoku-Oki
585 earthquake [36], and also located in a region of changes in the geometry of the subducted
586 slab. In the case of 2010 Maule earthquake, the pre-seismic mass decrease signal highlights
587 a larger amount of mass anomaly distributed over a more localized zone with a length com-
588 mensurate to that of the co-seismically ruptured area. We notice that the modelled Maule
589 pre-seismic normal faulting event should have generated centimetric surface displacements,
590 which have not been observed by GNSS [2]. This leads us to propose that part of this grav-
591 ity signal could reflect deep mass redistributions from large-scale fluid release promoted by
592 extensional cracks and normal faults in the subducted slab - even if it remains difficult to
593 decipher without ambiguity the physical processes at the origin of the gravity variations
594 observed prior these two earthquakes. Nevertheless, the existence of these interactions be-
595 tween slow mass variations at depth detected by GRACE and interplate seismicity, opens
596 a new field of research to better characterize and understand the dynamics of the seismic
597 cycle at megathrusts. Observing again such interactions for large earthquakes in the future
598 could lead to a paradigm shift in the study of the seismic cycle, which is today essentially
599 based on the distribution of the recurrence times of large earthquakes for the estimation
600 of the seismic hazard.

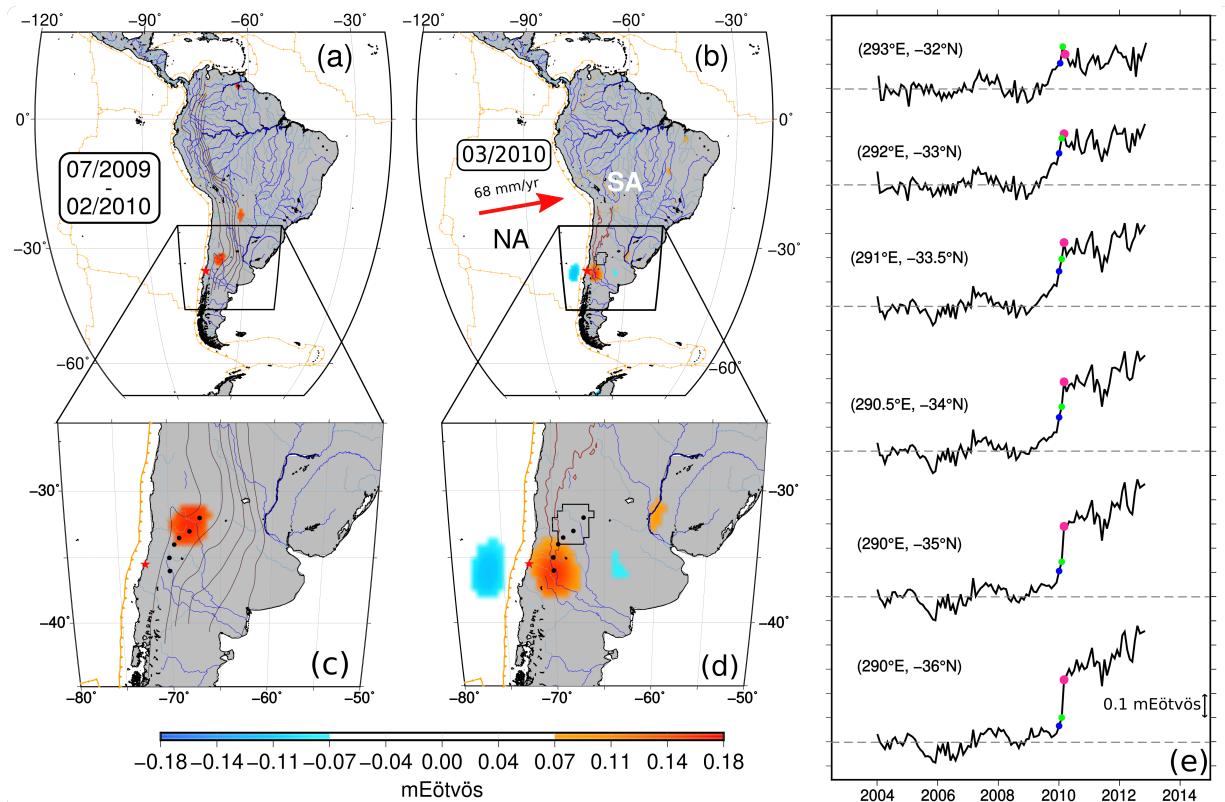


Figure 1: Pre-seismic and co-seismic gravity gradient signals for the Maule earthquake. All panels show the 800-km scale, $\phi\phi$ GRGS gravity gradients, stacked for -10 to 10° clockwise spherical frame rotations. Panels a and c: cumulated variation over the [July 2009 – February 2010] interval with an absolute amplitude above 0.07 mEötvös, also shown in black contours in the map d. Panels b and d: March 2010 co-seismic variations. Red star: Maule earthquake epicenter; orange lines: plate boundaries [3]; violet lines: Pacific slab isodepth contours every 100-km [16]; brown lines: 3000 m topographic contours. Tectonic plates: NA = Nazca, SA = South-America, Red arrow = subduction direction. Panel e: time series of the gravity gradients after removing the annual and semi-annual cycles and a trend, at locations spanning the pre- and co-seismic anomalies, shown as black dots in the maps c and d. Blue dot in the time series: January 2010 ; green dot: February 2010 ; pink dot: March 2010.

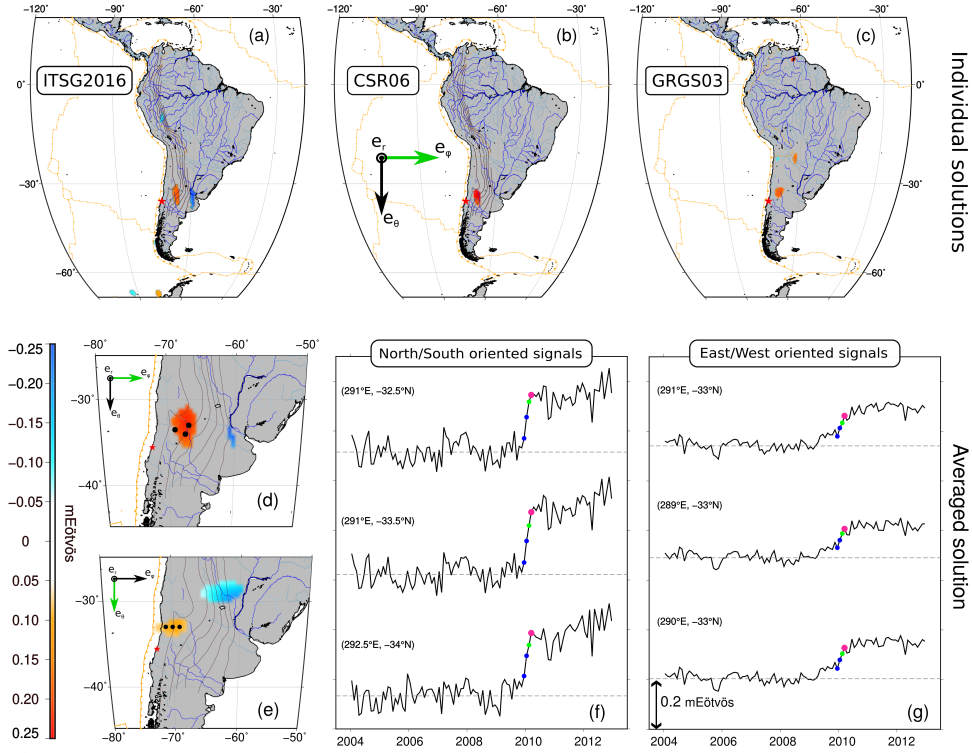


Figure 2: Anomalous gravity gradient signals before the Maule earthquake from the GRGS, CSR and ITSG-2016 gravity solutions and the average of the three solutions. Panels a-d and f : 800-km scale $\phi\phi$ gravity gradients in the local spherical frame, emphasizing North-South oriented signals. Panels e and g: 800-km scale $\theta\theta$ gravity gradients in the local spherical frame, emphasizing East-West oriented signals. Top panels: maps for each individual solution. Bottom line panels: maps and time series for the average of the three solutions. Panels a-e: Maps of anomalous gravity gradient signals in February 2010 (with a probability below 0.25% for ITSG-2016, below 1% for CSR, below $2.5 \cdot 10^{-5}\%$ for GRGS and below 0.01% for the average), persistent in time after March 2010 (see text). Panels f, g: time series of the gravity gradients at locations across the GRACE positive anomaly in February 2010, indicated by the black dots on the maps d, e respectively.

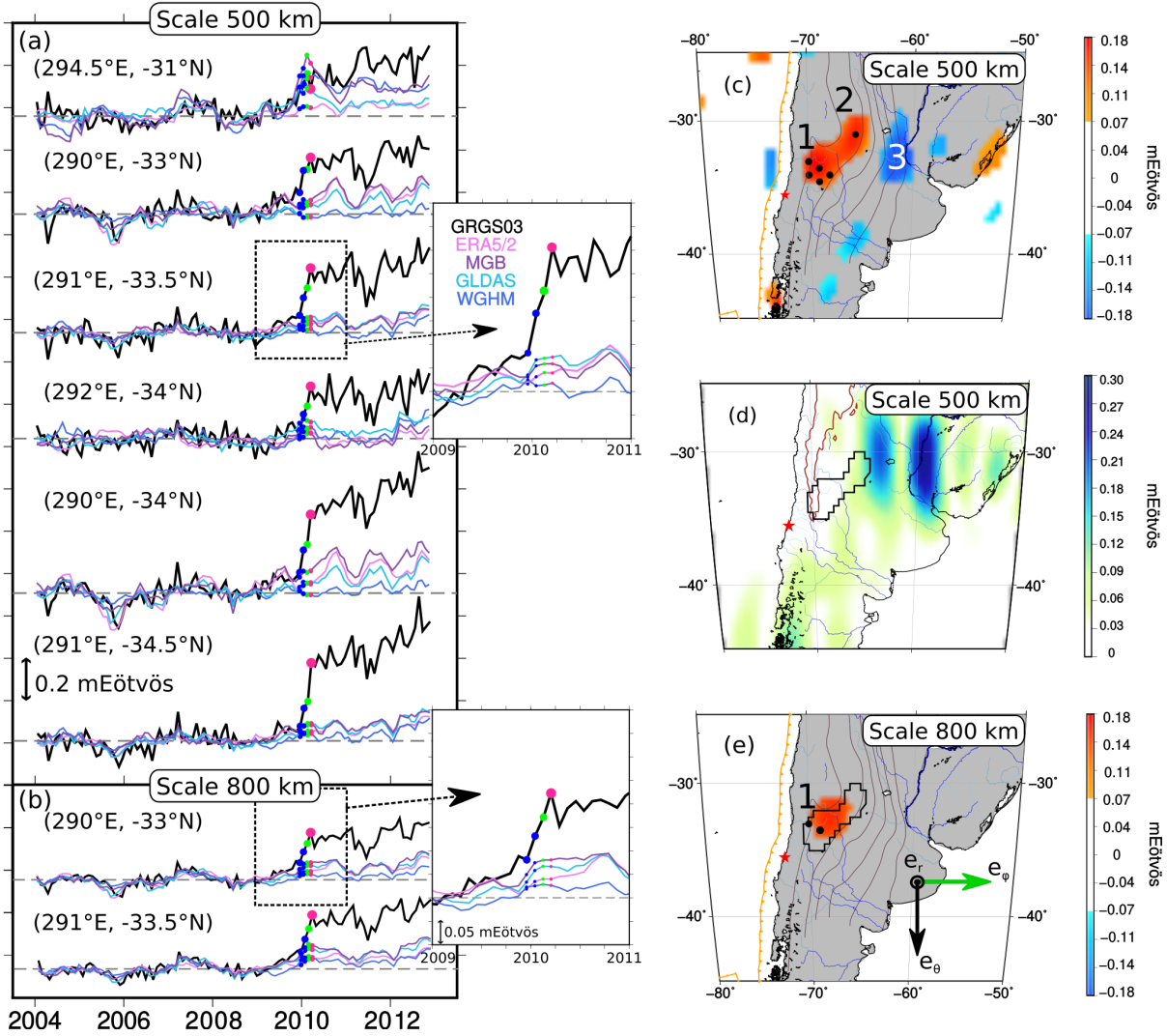


Figure 3: Comparison of the GRACE GRGS gravity gradient signals with those predicted from four hydrological models in the region of Maule at two spatial scales. Panels a,c and d: scale 500-km, $\phi\phi$ gradients in the local spherical frame. Panels b and e: scale 800-km, same gradients. Panels a (resp. b): time series at points across the GRACE GRGS positive anomaly before the earthquake, marked in black dots in the map c (resp. e). GRGS time series in black ; time series from the hydrological models in colors as referred in the zoomed panel a. The gravity gradients from the ERA5-Land hydrology model have been scaled by a factor 0.5 for consistency with the other hydrological models (Appendix S10). Panels c: Map of the GRACE GRGS anomalous signals before the earthquake. This map is derived from the same analysis as in Fig. 1a, considering a lower level of abnormality of the February 2010 signals (outside the 0.02 - 99.98 percentile range of the long-term distribution). Panel e: same as Fig. 1c. Panel d: Spatial patterns of the non-seasonal signals in the gravity gradients from the WGHM hydrological model, as expressed by the RMS of the 2009/09 – 2010/02 time series after subtraction of the annual, semi-annual and long-term trend components. For panels d and e, black lines are the contours of the positive GRACE GRGS anomaly shown in panel c.

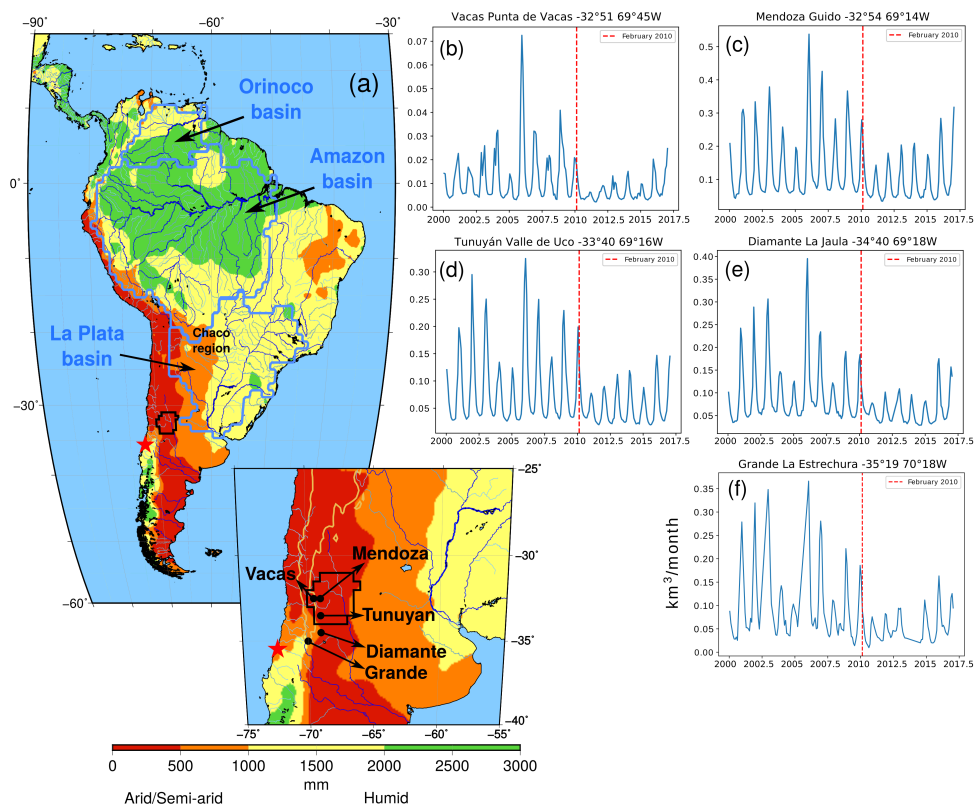


Figure 4: Panel a: map of the different climate zones of South America as reflected by the annual amount of precipitations [23], from arid/semi-arid to humid, superimposed with the contours of the GRACE pre-seismic signal of Fig. 1a (black lines). Panels b-f: monthly river discharge at hydrometric stations in the vicinity of the GRACE pre-seismic signal and upstream of the dams (black dots in the zoomed map of panel a), reflecting the annual supply of water in this arid region by snow and ice melting in the Andean Cordillera. Red dashed line: February 2010.

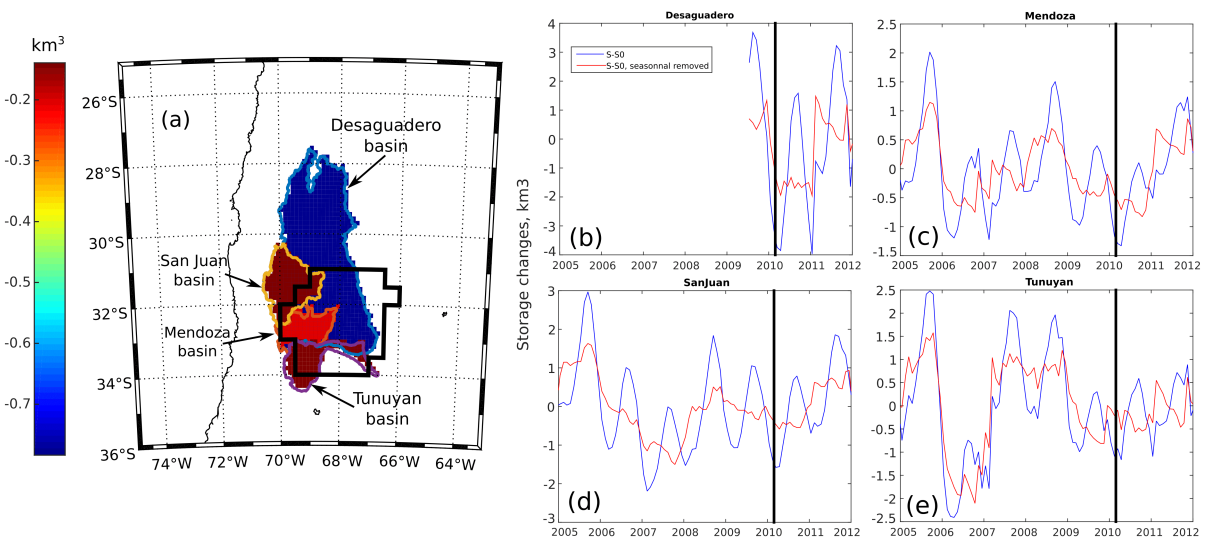


Figure 5: Estimated water storage variations of the Desaguadero, San Juan, Mendoza and Tunuyan basins in the region of Maule. Panel a: mass changes over the basins from the beginning of January to the end of February 2010, superimposed with the contour of the GRACE pre-seismic signal of Fig. 1a (black line). Panels b-e: time series of the water storage variations for each basin, before and after removing a seasonal cycle.

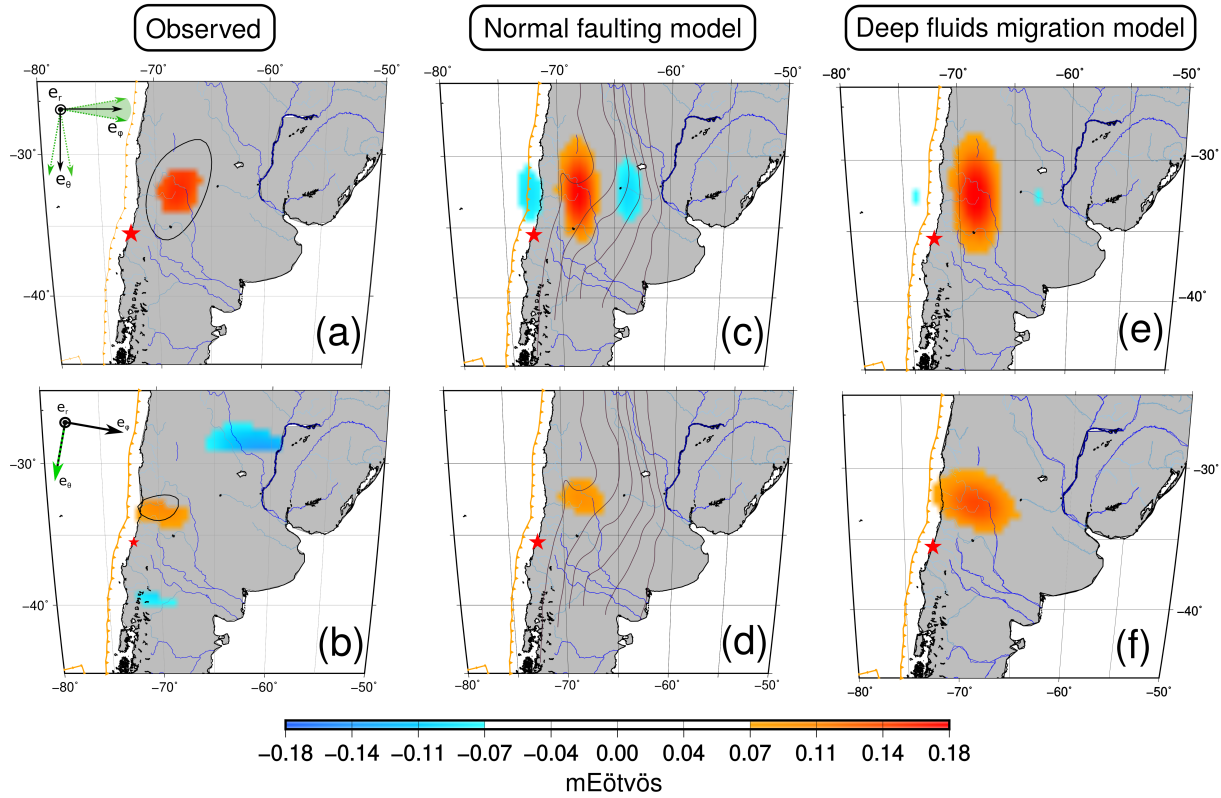


Figure 6: Comparison between the GRGS GRACE-observed (panels a-b) and the modeled (panels c-f) pre-seismic signals for the scale 800-km. Top panels: $\phi\phi$ gravity gradients, stacked for -10 to 10° clockwise spherical frame rotations ; Bottom panels: $\theta\theta$ gravity gradients for a 10° clockwise spherical frame rotation. Panel a: same as Fig.1c. The black lines depict the 0.10 mEötvös contours of the February 2010 gravity gradients. Panel b: same as Fig.1c for the considered $\theta\theta$ gravity gradients. Panels c-d: gravity gradient signals predicted from a model of quasi-static normal faulting in a vertically stratified elastic medium (see text). The violet lines are the slab isodepth contours every 100km [16]. Panels e-f: gravity gradient signals predicted from a model of density variations due to fluid infiltrations over a volume of $500 \times 500 \times 80$ -km at 150-km depth with porosity $\frac{\delta V}{V} = 5 \cdot 10^{-6}$ (see text).

601 Acknowledgments

602 This work was supported by CNES. It is based on observations from the GRACE satellites.
603 M.B. was funded by a CNES-IPGP fellowship. We thank Kerstin Schulze, Hannes Müller
604 Schmied and Petra Döll for providing us access to the WGHM hydrology model. We would
605 like to thank Ayan Fleischman, Nicolas Delbart, Emilie Lavie and Jean-Michel Lemoine for
606 their kind support and constructive discussions. Most figures of this paper were generated
607 using the free Generic Mapping Tools software (GMT) [50]. ~~This is IPGP contribution~~
608 ~~number XXX.~~

References

- [1] Megan L. Anderson, George Zandt, Enrique Triep, Matthew Fouch, and Susan Beck. Anisotropy and mantle flow in the Chile-Argentina subduction zone from shear wave splitting analysis: CHILE-ARGENTINA SUBDUCTION ZONE. Geophysical Research Letters, 31(23), December 2004.
- [2] Jonathan R. Bedford, Marcos Moreno, Zhiguo Deng, Onno Oncken, Bernd Schurr, Timm John, Juan Carlos Báez, and Michael Bevis. Months-long thousand-kilometre-scale wobbling before great subduction earthquakes. Nature Geoscience, 580:628–635, 2020.
- [3] Peter Bird. An updated digital model of plate boundaries. Geochemistry, Geophysics, Geosystems, 4(3), 2003. eprint: <https://agupubs.onlinelibrary.wiley.com/doi/pdf/10.1029/2001GC000252>.
- [4] Eva Boergens, Elena Rangelova, Michael G. Sideris, and Juergen Kusche. Assessment of the capabilities of the temporal and spatiotemporal ICA method for geophysical signal separation in GRACE data. Journal of Geophysical Research: Solid Earth, 119(5):4429–4447, May 2014.
- [5] Michel Bouchon, David Marsan, Virginie Durand, Michel Campillo, Hugo Perfettini, Raul Madariaga, and Blandine Gardonio. Potential slab deformation and plunge prior to the Tohoku, Iquique and Maule earthquakes. Nature Geoscience, 9(5):380–383, May 2016.
- [6] Thomas Cahill and Bryan L. Isacks. Seismicity and shape of the subducted Nazca Plate. Journal of Geophysical Research, 97(B12):17503, 1992.
- [7] Wenju Cai, Michael J. McPhaden, Alice M. Grimm, Regina R. Rodrigues, Andréa S. Taschetto, René D. Garreaud, Boris Dewitte, Germán Poveda, Yoo-Geun Ham, Agus Santoso, Benjamin Ng, Weston Anderson, Guojian Wang, Tao Geng,

634 Hyun-Su Jo, José A. Marengo, Lincoln M. Alves, Marisol Osman, Shujun Li, Lixin
635 Wu, Christina Karamperidou, Ken Takahashi, and Carolina Vera. Climate impacts
636 of the El Niño–Southern Oscillation on South America. Nature Reviews Earth &
637 Environment, 1(4):215–231, April 2020.

638 [8] B. F. Chao and J. R. Liao. Gravity Changes Due to Large Earthquakes Detected
639 in GRACE Satellite Data via Empirical Orthogonal Function Analysis. Journal of
640 Geophysical Research: Solid Earth, 124(3):3024–3035, March 2019.

641 [9] Chunli Dai, C. K. Shum, Junyi Guo, Kun Shang, Byron Tapley, and Rongjiang Wang.
642 Improved source parameter constraints for five undersea earthquakes from north com-
643 ponent of GRACE gravity and gravity gradient change measurements. Earth and
644 Planetary Science Letters, 443:118–128, June 2016.

645 [10] D. P. Dee, S. M. Uppala, A. J. Simmons, P. Berrisford, P. Poli, S. Kobayashi, U. An-
646 drae, M. A. Balmaseda, G. Balsamo, P. Bauer, P. Bechtold, A. C. M. Beljaars,
647 L. van de Berg, J. Bidlot, N. Bormann, C. Delsol, R. Dragani, M. Fuentes, A. J.
648 Geer, L. Haimberger, S. B. Healy, H. Hersbach, E. V. Hólm, L. Isaksen, P. Kållberg,
649 M. Köhler, M. Matricardi, A. P. McNally, B. M. Monge-Sanz, J.-J. Morcrette, B.-K.
650 Park, C. Peubey, P. de Rosnay, C. Tavolato, J.-N. Thépaut, and F. Vitart. The ERA-
651 Interim reanalysis: configuration and performance of the data assimilation system.
652 Quarterly Journal of the Royal Meteorological Society, 137(656):553–597, April 2011.

653 [11] Bertrand Delouis, Jean-Mathieu Nocquet, and Martin Vallée. Slip distribution of the
654 february 27, 2010 mw= 8.8 maule earthquake, central chile, from static and high-rate
655 gps, insar, and broadband teleseismic data. Geophysical Research Letters, 37(17),
656 2010.

657 [12] Besim Dragovic, Ethan F. Baxter, and Mark J. Caddick. Pulsed dehydration and
658 garnet growth during subduction revealed by zoned garnet geochronology and thermo-
659 dynamic modeling, Sifnos, Greece. Earth and Planetary Science Letters, 413:111–122,
660 March 2015.

- 661 [13] Caroline M. Eakin, Maureen D. Long, Alissa Scire, Susan L. Beck, Lara S. Wag-
662 ner, George Zandt, and Hernando Tavera. Internal deformation of the subducted
663 Nazca slab inferred from seismic anisotropy. Nature Geoscience, 9(1):56–59, Jan-
664 uary 2016. Bandiera_abtest: a Cg_type: Nature Research Journals Number: 1
665 Primary_atype: Research Publisher: Nature Publishing Group Subject_term: Geo-
666 dynamics;Seismology;Tectonics Subject_term_id: geodynamics;seismology;tectonics.
- 667 [14] René D. Garreaud, Camila Alvarez-Garretón, Jonathan Barichivich, Juan Pablo
668 Boisier, Duncan Christie, Mauricio Galleguillos, Carlos LeQuesne, James McPhee,
669 and Mauricio Zambrano-Bigiarini. The 2010–2015 megadrought in central Chile: im-
670 pacts on regional hydroclimate and vegetation. Hydrology and Earth System Sciences,
671 21(12):6307–6327, December 2017.
- 672 [15] Shin-Chan Han, Jeanne Sauber, and Scott Luthcke. Regional gravity de-
673 crease after the 2010 Maule (Chile) earthquake indicates large-scale mass
674 redistribution. Geophysical Research Letters, 37(23), 2010. _eprint:
675 <https://agupubs.onlinelibrary.wiley.com/doi/pdf/10.1029/2010GL045449>.
- 676 [16] Gavin P. Hayes, Ginevra L. Moore, Daniel E. Portner, Mike Hearne, Hanna Flamme,
677 Maria Furtney, and Gregory M. Smoczyk. Slab2, a comprehensive subduction zone
678 geometry model. Science, 362(6410):58–61, October 2018.
- 679 [17] Kosuke Heki and Koji Matsuo. Coseismic gravity changes of the 2010 earthquake
680 in central Chile from satellite gravimetry: COSEISMIC GRAVITY CHANGES IN
681 CHILE. Geophysical Research Letters, 37(24):n/a–n/a, December 2010.
- 682 [18] Matthias Holschneider, Aude Chambodut, and Mioara Mandea. From global to re-
683 gional analysis of the magnetic field on the sphere using wavelet frames. Physics of
684 the Earth and Planetary Interiors, 135(2-3):107–124, February 2003.

- 685 [19] Erik R. Ivins and Charles G. Sammis. Transient creep of a composite lower crust: 1.
686 Constitutive theory. Journal of Geophysical Research: Solid Earth, 101(B12):27981–
687 28004, December 1996.
- 688 [20] Timm John, Nikolaus Gussone, Yuri Y Podladchikov, Gray E Bebout, Ralf Dohmen,
689 Ralf Halama, Reiner Klemd, Tomas Magna, and Hans-Michael Seitz. Volcanic arcs fed
690 by rapid pulsed fluid flow through subducting slabs. Nature Geoscience, 5(7):489–492,
691 2012.
- 692 [21] Martin Jung, Markus Reichstein, Philippe Ciais, Sonia I. Seneviratne, Justin Sheffield,
693 Michael L. Goulden, Gordon Bonan, Alessandro Cescatti, Jiquan Chen, Richard
694 de Jeu, A. Johannes Dolman, Werner Eugster, Dieter Gerten, Damiano Gianelle,
695 Nadine Gobron, Jens Heinke, John Kimball, Beverly E. Law, Leonardo Montagnani,
696 Qiaozhen Mu, Brigitte Mueller, Keith Oleson, Dario Papale, Andrew D. Richardson,
697 Olivier Roupsard, Steve Running, Enrico Tomelleri, Nicolas Viovy, Ulrich Weber,
698 Christopher Williams, Eric Wood, Sönke Zaehle, and Ke Zhang. Recent decline in
699 the global land evapotranspiration trend due to limited moisture supply. Nature,
700 467(7318):951–954, October 2010.
- 701 [22] T. Lay, C. J. Ammon, H. Kanamori, K. D. Koper, O. Sufri, and A. R.
702 Hutko. Teleseismic inversion for rupture process of the 27 February 2010 Chile
703 (Mw 8.8) earthquake. Geophysical Research Letters, 37(13), 2010. _eprint:
704 <https://agupubs.onlinelibrary.wiley.com/doi/pdf/10.1029/2010GL043379>.
- 705 [23] David R. Legates and Cort J. Willmott. Mean seasonal
706 and spatial variability in gauge-corrected, global precipitation.
707 International Journal of Climatology, 10(2):111–127, 1990. _eprint:
708 <https://rmets.onlinelibrary.wiley.com/doi/pdf/10.1002/joc.3370100202>.
- 709 [24] Jean-Michel Lemoine, Sean Bruinsma, Sylvain Loyer, Richard Biancale, Jean-Charles
710 Marty, Felix Perosanz, and Georges Balmino. Temporal gravity field models inferred
711 from GRACE data. Advances in Space Research, 39(10):1620–1629, January 2007.

- 712 [25] Yu-nung Nina Lin, Anthony Sladen, Francisco Ortega-Culaciati, Mark Simons, Jean-
713 Philippe Avouac, Eric J. Fielding, Benjamin A. Brooks, Michael Bevis, Jeff Genrich,
714 Andreas Rietbrock, Christophe Vigny, Robert Smalley, and Anne Socquet. Coseismic
715 and postseismic slip associated with the 2010 Maule Earthquake, Chile: Characteriz-
716 ing the Arauco Peninsula barrier effect: CHARACTERIZING ARAUCO BARRIER
717 EFFECT. Journal of Geophysical Research: Solid Earth, 118(6):3142–3159, June
718 2013.
- 719 [26] Di Long, Laurent Longuevergne, and Bridget R. Scanlon. Uncertainty in
720 evapotranspiration from land surface modeling, remote sensing, and GRACE
721 satellites. Water Resources Research, 50(2):1131–1151, 2014. _eprint:
722 <https://onlinelibrary.wiley.com/doi/pdf/10.1002/2013WR014581>.
- 723 [27] S. Lorito, F. Romano, S. Atzori, X. Tong, A. Avallone, J. McCloskey, M. Cocco,
724 E. Boschi, and A. Piatanesi. Limited overlap between the seismic gap and coseismic
725 slip of the great 2010 Chile earthquake. Nature Geoscience, 4(3):173–177, March 2011.
- 726 [28] Colton Lynner, Megan L. Anderson, Daniel E. Portner, Susan L. Beck, and Hersh
727 Gilbert. Mantle flow through a tear in the Nazca slab inferred from shear wave
728 splitting. Geophysical Research Letters, 44(13):6735–6742, July 2017.
- 729 [29] Mariano H. Masiokas, Ricardo Villalba, Brian H. Luckman, Carlos Le Quesne, and
730 Juan Carlos Aravena. Snowpack Variations in the Central Andes of Argentina and
731 Chile, 1951–2005: Large-Scale Atmospheric Influences and Implications for Water
732 Resources in the Region. Journal of Climate, 19(24):6334–6352, December 2006.
- 733 [30] Torsten Mayer-Gürr, Saniya Behzadpour, Matthias Ellmer, Beate Klinger, Andreas
734 Kvas, and Norbert Zehentner. ITSG-Grace2016 - Monthly and Daily Gravity Field
735 Solutions from GRACE. 2016.

- 736 [31] Marianne Metois, C Vigny, and A Socquet. Interseismic coupling, megathrust earth-
737 quakes and seismic swarms along the Chilean subduction zone (38–18 s). Pure and
738 Applied Geophysics, 173(5):1431–1449, 2016.
- 739 [32] Stella M. Moreiras. Climatic effect of ENSO associated with landslide occurrence in
740 the Central Andes, Mendoza Province, Argentina. Landslides, 2(1):53–59, April 2005.
- 741 [33] Marcos Moreno, Matthias Rosenau, and Onno Oncken. 2010 Maule earthquake slip
742 correlates with pre-seismic locking of Andean subduction zone. Nature, 467(7312):198–
743 202, September 2010.
- 744 [34] Hannes Müller Schmied, Denise Cáceres, Stephanie Eisner, Martina Flörke, Claudia
745 Herbert, Christoph Niemann, Thedini Asali Peiris, Eklavya Popat, Felix Theodor
746 Portmann, Robert Reinecke, et al. The global water resources and use model wa-
747 tergap v2. 2d: model description and evaluation. Geoscientific Model Development,
748 14(2):1037–1079, 2021.
- 749 [35] Isabelle Panet. An Analysis of Gravitational Gradients in Rotated Frames and Their
750 Relation to Oriented Mass Sources. Journal of Geophysical Research: Solid Earth,
751 123(12):11,062–11,090, December 2018.
- 752 [36] Isabelle Panet, Sylvain Bonvalot, Clément Narteau, Dominique Remy, and Jean-
753 Michel Lemoine. Migrating pattern of deformation prior to the Tohoku-Oki earthquake
754 revealed by GRACE data. Nature Geoscience, 11(5):367–373, May 2018.
- 755 [37] Oliver Plümper, Timm John, Yuri Y Podladchikov, Johannes C Vrijmoed, and Marco
756 Scambelluri. Fluid escape from subduction zones controlled by channel-forming reac-
757 tive porosity. Nature Geoscience, 10(2):150–156, 2017.
- 758 [38] Daniel Evan Portner, Susan Beck, George Zandt, and Alissa Scire. The nature of sub-
759 slab slow velocity anomalies beneath South America. Geophysical Research Letters,
760 44(10):4747–4755, May 2017.

- 761 [39] M. Rodell, P. R. Houser, U. Jambor, J. Gottschalck, K. Mitchell, C.-J. Meng, K. Ar-
762 senault, B. Cosgrove, J. Radakovich, M. Bosilovich, J. K. Entin, J. P. Walker,
763 D. Lohmann, and D. Toll. The Global Land Data Assimilation System. Bulletin
764 of the American Meteorological Society, 85(3):381–394, March 2004.
- 765 [40] Bruno Rudolf. The Global Precipitation Climatology Centre (GPCC). page 17.
- 766 [41] S. Ruiz and R. Madariaga. Historical and recent large megathrust earthquakes in
767 Chile. Tectonophysics, 733:37–56, May 2018.
- 768 [42] Himanshu Save, Byron Tapley, and Srinivas Bettadpur. GRACE RL06 reprocessing
769 and results from CSR. page 10697, April 2018. Conference Name: EGU General
770 Assembly Conference Abstracts.
- 771 [43] U Schneider, A Becker, P Finger, E Rustemeier, and M Ziese. Gpcc full data monthly
772 product version 2020 at 0.25°: monthly land-surface precipitation from rain-gauges
773 built on gts-based and historical data. Global Precipitation Climatology Centre at
774 Deutscher Wetterdienst: Offenbach, Germany, 2020.
- 775 [44] Vinícius A. Siqueira, Rodrigo C. D. Paiva, Ayan S. Fleischmann, Fernando M. Fan,
776 Anderson L. Ruhoff, Paulo R. M. Pontes, Adrien Paris, Stéphane Calmant, and Walter
777 Collischonn. Toward continental hydrologic–hydrodynamic modeling in South Amer-
778 ica. Hydrology and Earth System Sciences, 22(9):4815–4842, September 2018.
- 779 [45] Stephan Taetz, Timm John, Michael Bröcker, Carl Spandler, and Andreas Stracke.
780 Fast intraslab fluid-flow events linked to pulses of high pore fluid pressure at the
781 subducted plate interface. Earth and Planetary Science Letters, 482:33–43, 2018.
- 782 [46] Yusaku Tanaka and Kosuke Heki. Long- and short-term postseis-
783 mic gravity changes of megathrust earthquakes from satellite gravime-
784 try. Geophysical Research Letters, 41(15):5451–5456, 2014. _eprint:
785 <https://agupubs.onlinelibrary.wiley.com/doi/pdf/10.1002/2014GL060559>.

- 786 [47] B. D. Tapley. GRACE Measurements of Mass Variability in the Earth System. Science,
787 305(5683):503–505, July 2004.
- 788 [48] A. Udias, R. Madariaga, E. Buforn, D. Munoz, and M. Ros. The Large Chilean
789 Historical Earthquakes of 1647, 1657, 1730, and 1751 from Contemporary Documents.
790 Bulletin of the Seismological Society of America, 102(4):1639–1653, August 2012.
- 791 [49] Lei Wang, C. K. Shum, Frederik J. Simons, Andrés Tassara, Kamil Erkan, Christopher
792 Jekeli, Alexander Braun, Chungyen Kuo, Hyongki Lee, and Dah-Ning Yuan. Coseismic
793 slip of the 2010 Mw 8.8 Great Maule, Chile, earthquake quantified by the inversion
794 of GRACE observations. Earth and Planetary Science Letters, 335-336:167–179, June
795 2012.
- 796 [50] Paul Wessel and Walter HF Smith. New version of the generic mapping tools. Eos,
797 Transactions American Geophysical Union, 76(33):329–329, 1995.

799 A Gravity gradients at different spatial scales

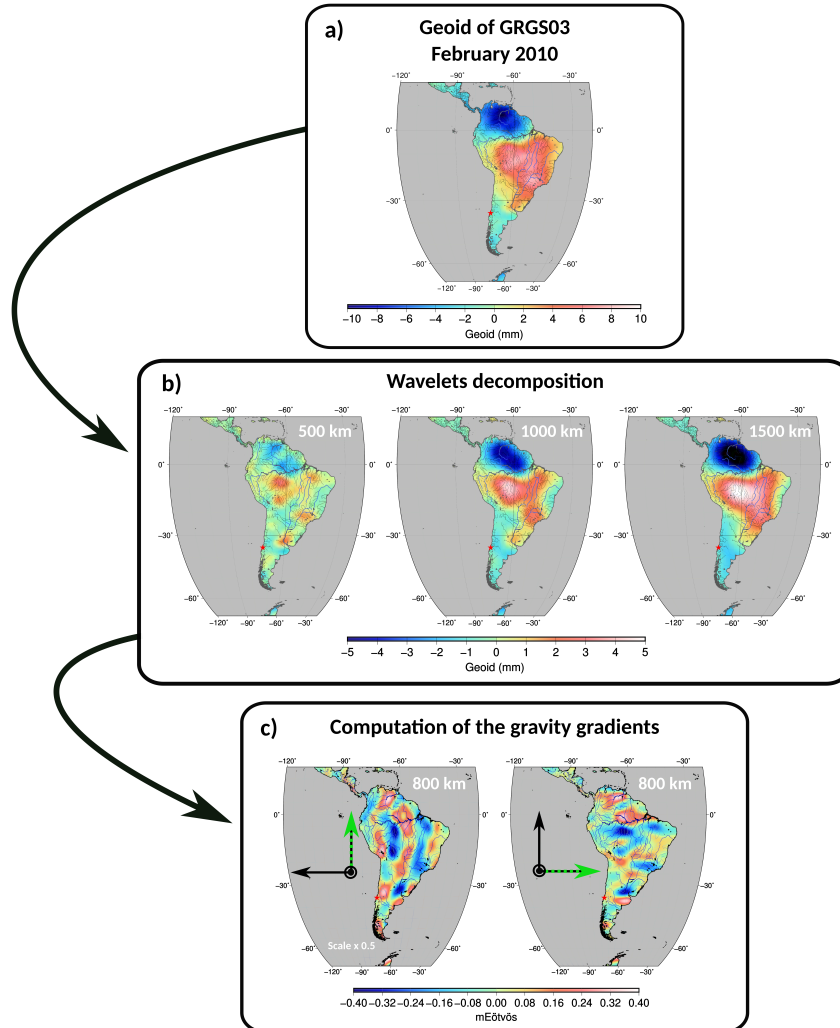


Figure S1: From the geoid to the multi-scale gravity gradients. Panel a: February 2010 geoid map (GRGS gravity solution). Panel b: wavelet analysis of the geoid map shown in Panel a, at different spatial scales (500, 1000 and 1500-km). Panel c: second-order gradients of the 800-km scale wavelet-filtered geopotential. In the spherical approximation, the geopotential is proportional to the geoid. Left (resp. right) panel: $\phi\phi$ (resp. $\theta\theta$) gravity gradients in the local south-east-up spherical frame.

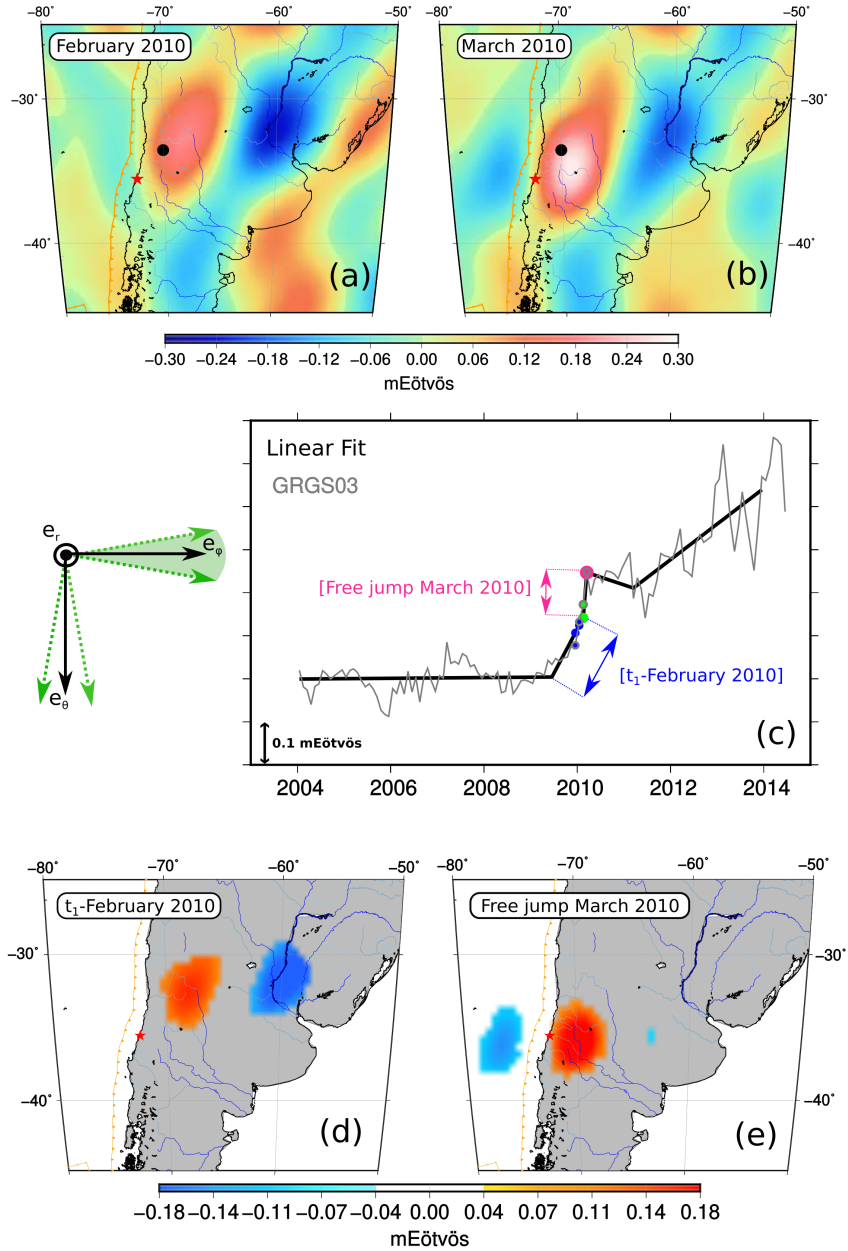


Figure S2: Piece-wise linear fit of the time series of the GRGS gravity gradients (800-km scale, $\phi\phi$ gravity gradients in the local south-east-up spherical frame, averaged for -10° to 10° clockwise frame rotations around the radial axis). Panel a-b: maps of the monthly gravity gradients in February and March 2010. Panel c: time series at the location marked by a black dot in the Panels a-b (thin grey line) and their piece-wise linear model (thick black line). Panel e d: cumulated variation over the [July 2009 - February 2010] interval, associated with abnormally large signals in February 2010 (probability below $2.5 \cdot 10^{-4}\%$) with an amplitude threshold of 0.1 mEötvös on the eight months trend. Panel d e: March 2010 co-seismic signal, associated with abnormally large signals in March 2010 (probability below $2.5 \cdot 10^{-4}\%$). Here, the level of abnormality of the February and March 2010 signals is lower than in Main Fig. 1.

800 **B Wavelet filtering of the geoid**

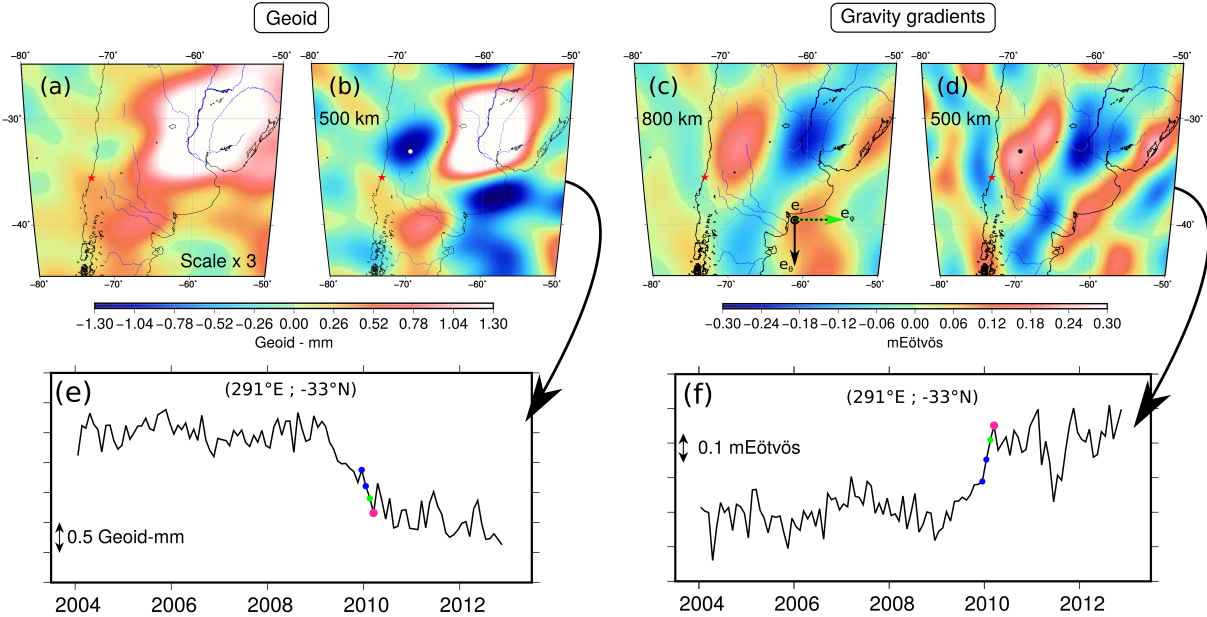


Figure S3: Comparison between the total geoid, the wavelet-filtered geoid and the multi-scale gravity gradients in February 2010 (GRGS gravity solution). Panel a: February 2010 geoid anomaly map. Panel b: 500-km scale wavelet analysis of the geoid, using the same wavelets as for the computation of the multi-scale gravity gradients. Panels c (resp. d): 500-km scale (resp. 800-km scale) $\phi\phi$ gravity gradients in the local South-East-Up spherical frame, emphasizing North-South oriented signals in February 2010. Panel e (resp. f): time serie at the location indicated by the white (resp. black) dot on the maps b (resp. d).

801 Fig. S3 compares the February 2010 signals in the studied region, as obtained from the
 802 total geoid, from the wavelet-filtered geoid and from the horizontal $\phi\phi$ gravity gradients.
 803 The contribution of the major hydrological sources from the La Plata basin predominates
 804 in the total geoid (Fig. S3a), partially masking the Maule pre-seismic signal. This smaller
 805 signal is emphasized in a high-resolution wavelet filtering of the geoid (Fig. S3b) and can
 806 be detected in the corresponding time series (Fig. S3e). However, it is not well separated
 807 from the nearby La Plata anomaly, which still perturbs the amplitude of the 500-km scale
 808 geoid signal in the region of the pre-seismic anomaly. The horizontal gravity gradients
 809 perform a better separation of these two signals, as shown by the comparison of the panel
 810 b with the panels c and d, where the amplitude of the La Plata anomaly has considerably

811 decreased and that of the Maule pre-seismic signal starts to predominate. Indeed, the La
812 Plata signal has a strong East-West component, which is filtered out in the North-South
813 oriented gravity gradients.

814 C Temporal unicity of the GRGS pre-seismic signal

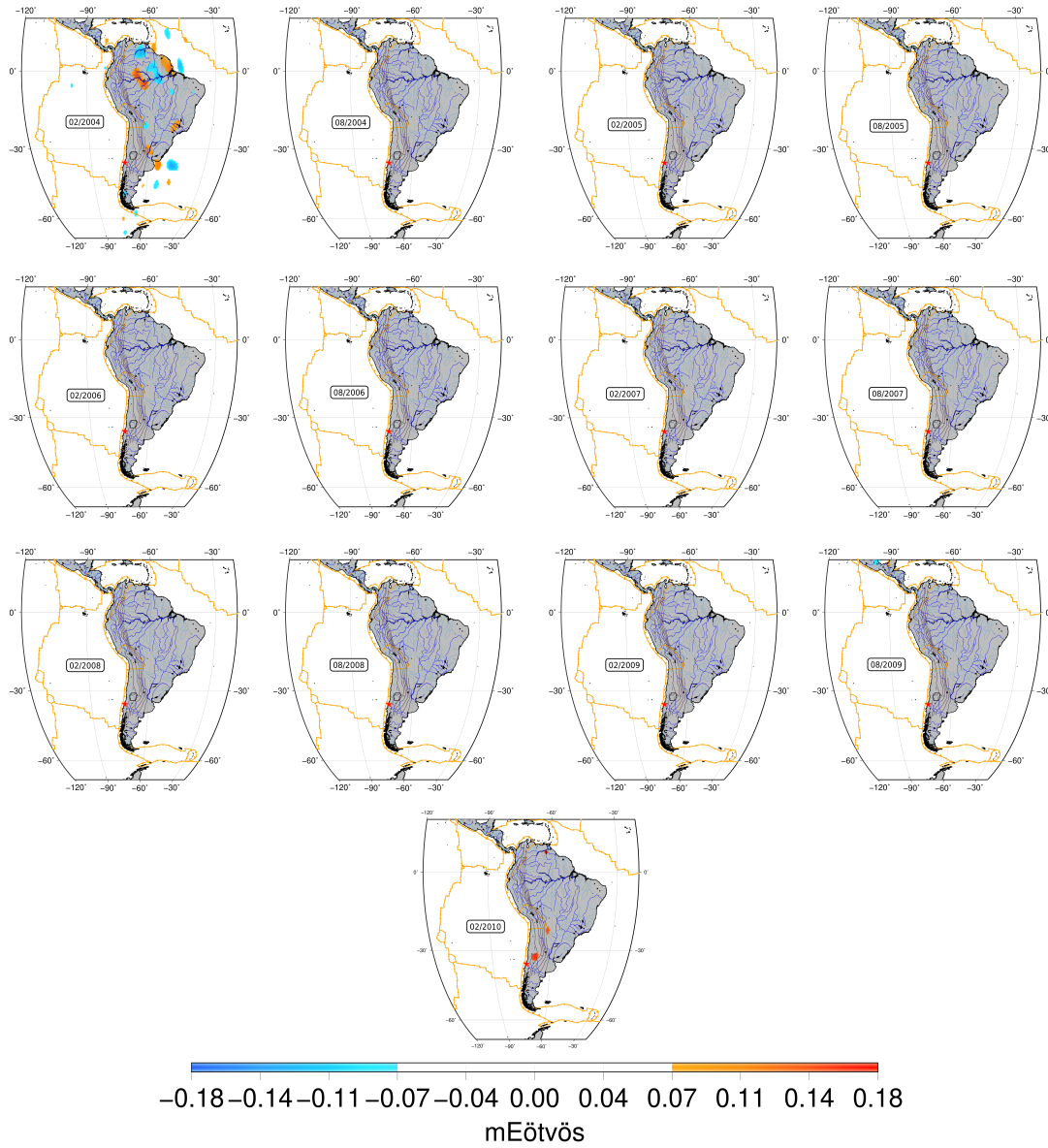


Figure S4: Time series of anomalous gravity gradient signals over South America obtained by applying the same analysis as in Fig. 1a, for hypothetical earthquake times t_e spanning the [January 2003 – March 2010] time interval. Same scale and orientations of the spherical frame as in Fig. 1.

815 D Investigation of other GRACE solutions

816 D.1 Signal in individual solutions

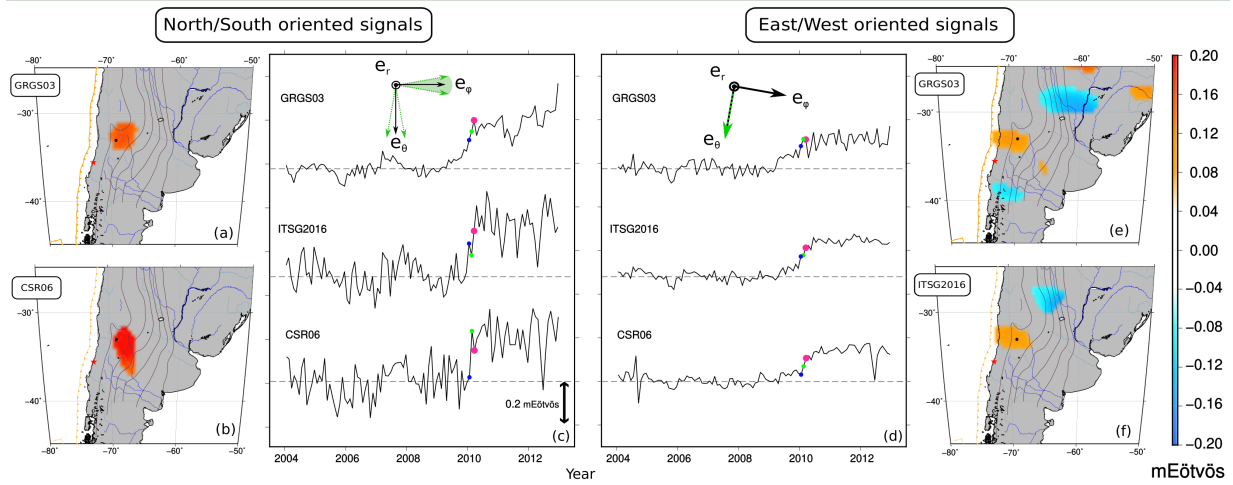


Figure S5: Comparison of the gravity gradient signals before the Maule earthquake from three different gravity field solutions: GRGS, CSR and ITSG-2016. Panels a-c (resp. panels d-f): 800-km scale $\phi\phi$ (resp. $\theta\theta$) gravity gradients in the local south-east-up spherical frame, emphasizing North-South (resp. East-West) oriented signals. The time series at the point $(-33^\circ\text{N}; 291^\circ\text{E})$ marked by a black dot on all maps, are compared in panels c-d for each gravity solution and each orientation. Maps a-b compare the spatial patterns of pre-seismic gravity gradient anomalies in the GRGS and the CSR solutions, for the North-South orientation. Maps e-f show the same comparison for the East-West orientation, between the GRGS and the ITSG-2016 solutions. For the GRGS solutions, the spatial signals in the maps a,e are obtained in the same way as in Fig. 1a. For the CSR and ITSG-2016 solutions, the maps represent abnormally large values in February 2010, outside of the [1-99%] (CSR) and the [2.5-97.5%] (ITSG-2016) percentiles of the long-term distributions of the time series, persistent in time after March 2010 (see Main Text, section 3.3).

817 D.2 Singular Value Decomposition of coupled fields

818 D.2.1 Principle

819 To identify common spatio-temporal patterns between the three gravity models (GRGS,
820 ITSG and CSR) taken two-by-two, we used a singular value decomposition (SVD). This
821 method is well-suited to identify the coupled space-time patterns of variability between
822 two fields. It is based on the decomposition of the cross-covariance matrix of the two
823 space-time data matrices into a linear combination of orthogonal modes, each expressed
824 by the multiplication of a spatial pattern with a time series. In more detail, the principle
825 is as follows. We first construct the temporal cross-covariance matrix (C) between two
826 data fields e.g. GRGS (G) and ITSG (I). Each data field is represented by a rectangular
827 $n \times p$ matrix, where n is the number of epochs and p the number of locations (grid points
828 in the case of a regular grid), such that $G_{ij} = g_{\text{GRGS}}(t_i, r_j)$ for the GRGS03 solution,
829 $I_{ij} = g_{\text{ITSG}}(t_i, r_j)$ for the ITSG solution. Here, t_i denotes the i -th epoch, r_j the j -th
830 position on the spatial grid, g_{GRGS} (resp. g_{ITSG}) denotes the GRGS (resp. ITSG) gravity
831 gradients. We have:

$$C = \text{cov}(G, I) = G^t I \quad (1)$$

832 Then, we compute the SVD of the cross-covariance matrix C by solving the following equa-
833 tion, which can be seen as a generalization to rectangular matrices of the diagonalization
834 of the square symmetric matrix:

$$C = ULV^t. \quad (2)$$

835 We obtain two sets of spatially orthogonal singular vectors (the columns of U and V
836 for matrices G and I respectively). The diagonal matrix L contains the singular values
837 associated with each pair of singular vectors. Each common mode is represented by the
838 product between a temporal mode $a(t)$ and its associated spatial mode $b(r)$. The i -th
839 temporal mode is given by the i -th column of the matrix $A = GU$ (resp. $B = IV$) for the
840 GRGS data field (resp. the ITSG data field). The associated spatial patterns are given by
841 the i -th columns of U and V respectively. Finally, the importance of each common mode

842 is reflected by the fraction of the squared covariance explained by this mode (SCF_k). For
843 the k^{th} common mode, it is given by: $SCF_k = \frac{L(k,k)}{\text{trace}(L)}$.

844 **D.2.2 Results**

845 In the North-South direction, the first common modes between GRGS and CSR, and be-
846 tween GRGS and ITSG-2016, represent more than 75 % of the squared covariance between
847 each pair of solutions, in both cases (Fig. S6c,k). Thus, they point to a highly coupled
848 behaviour of each pair of solutions. The associated spatial pattern covers the locations
849 of the co-seismic and pre-seismic signals (Fig. S6a,b,i,j); the temporal pattern shows a
850 progressive increase in the gravity gradients over three months up to March 2010, in each
851 gravity gradient solution (Fig. S6d,l). In the East-West direction, the first common modes
852 explain a smaller amount of variance, at the level of 50 % of covariance (Fig. S6g,o) -
853 which is still relatively high. This is due to a larger contribution of the hydrological signals
854 in the La Plata basin in this direction, in the 2^{nd} mode. The spatial and temporal patterns
855 of this mode are consistent with those obtained in the North-South direction: the spatial
856 pattern is localized in the epicentral region (Fig. S6e,f,m,n), and the temporal evolution
857 shows a progressive step-like variation initiated months before the rupture, stabilized in
858 March 2010 (Fig. S6h,p).

859

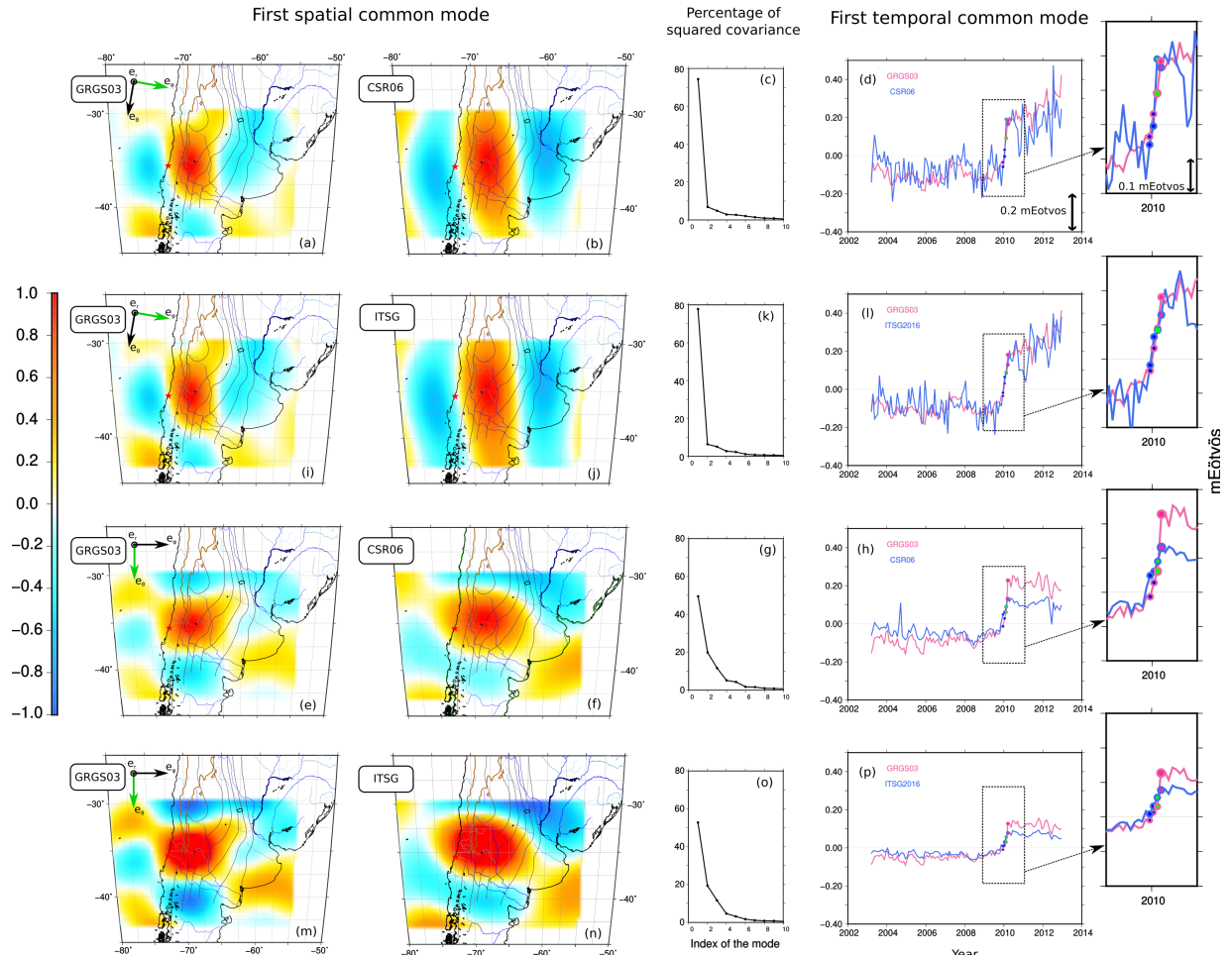


Figure S6: Common modes of variability in the region of Maule between the 800-km scale GRGS gravity gradients and the 800-km scale CSR (top and lower middle lines) or ITSG-2016 (upper middle and bottom lines) gravity gradients respectively, in the North-South direction ($\phi\phi$ gradients in the local spherical frame, top two lines) and in the East-West direction ($\theta\theta$ gradients in the local spherical frame, bottom two lines). Columns 1 and 2: non-dimensionalized spatial pattern of the first common mode for each gravity gradient solution ; column 3: percentage of covariance explained ; column 4: dimensionalized time series of the first common mode for each gravity gradient solution. Blue dot in the time series: January 2010 ; green dot: February 2010 ; pink dot: March 2010.

E Hydrological models and in-situ data

To separate solid Earth and hydrological signals, we designed both a model-driven and a data-driven approach to define the impact of water redistribution on gravity. We considered four complementary hydrological models: 1. The global GLDAS NOAH 2.1 model (including soil moisture, snow and water stored in the canopy) at 0.25° resolution [39], 2. the global WGHM model (including soil moisture, snow, groundwater and surface water) at 0.5° resolution [34], 3. the global ERA5-Land model at 9-km resolution (including soil moisture and snow) [10] and 4. the regional MGB model for South America (including canopy, soil moisture, ground water and surface water) at 10-km resolution [44]. We reconstructed each month the geoid and the gravity gradients predicted by these different models, considering the direct newtonian attraction of the water loads and applying a thin layer approximation. Here, the model ensemble is used to better quantify errors arising from forcing data, model structure, and model spatial resolution. Then, we use the gravity gradient signals predicted from these models for comparisons with the observed ones, in order to discuss the origin of the GRACE anomalies. Comparing these four different models also allow us to identify robust features and model-dependent errors arising from forcing data, model structure, and model spatial resolution.

In specific regions, we complete the model analysis with water storage changes inferred from in-situ observations. We considered observations of river discharge (Q), precipitation (P) and actual evapotranspiration (E). The precipitation is based on the Global Precipitation Climatology Center (GPCC) “Full Data Monthly Version 2020” dataset [43]. The GPCC provides gridded gauge-analysis products derived from quality controlled station data, at 0.25° resolution [40]. The actual evapotranspiration is provided by the Max Planck Institute [21]. It is estimated from a data-driven approach, based on a global monitoring network, meteorological and remote-sensing observations, and a machine-learning algorithm. Finally, we used river discharge data and basin outlines provided by the Global Runoff Data Centre (GRDC). The hydrological analysis is performed over 2005-2012 when

888 discharge data is available, in order to remove properly ~~an~~ annual and semi-annual signals.
889 Furthermore, in order to remove the potential impact of systematic bias in the fluxes data
890 (e.g. [26]), a linear trend is fitted on water storage changes over the 2005-2012 period.

891

892 F Hydrological context map

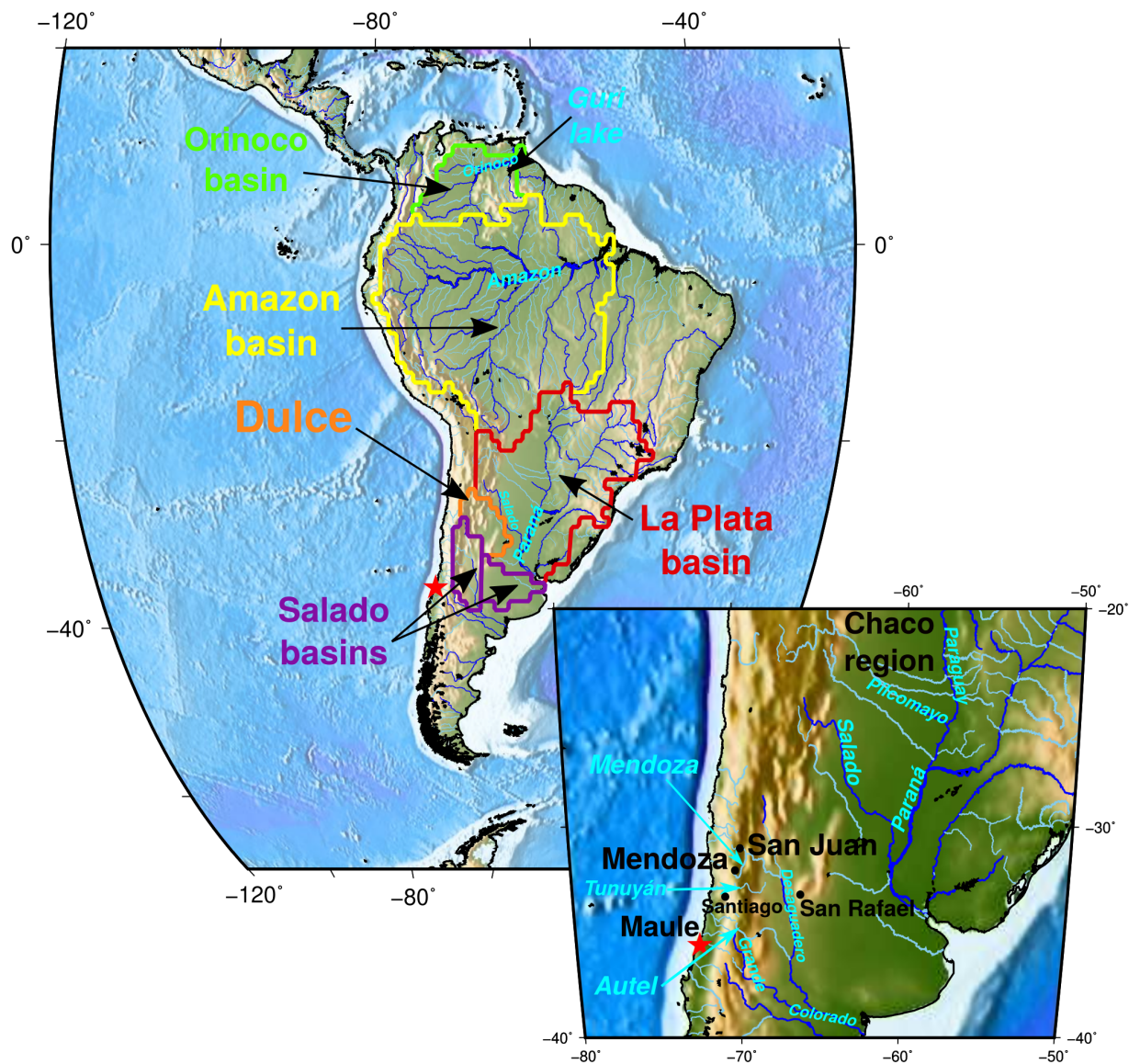


Figure S7: Map of the hydrological drainage basins in South America. The rivers names are written in blue, cities and regions in black.

893 **G Non-seasonal variability of the hydrological models**

894 **G.1 6 months period before the earthquake**

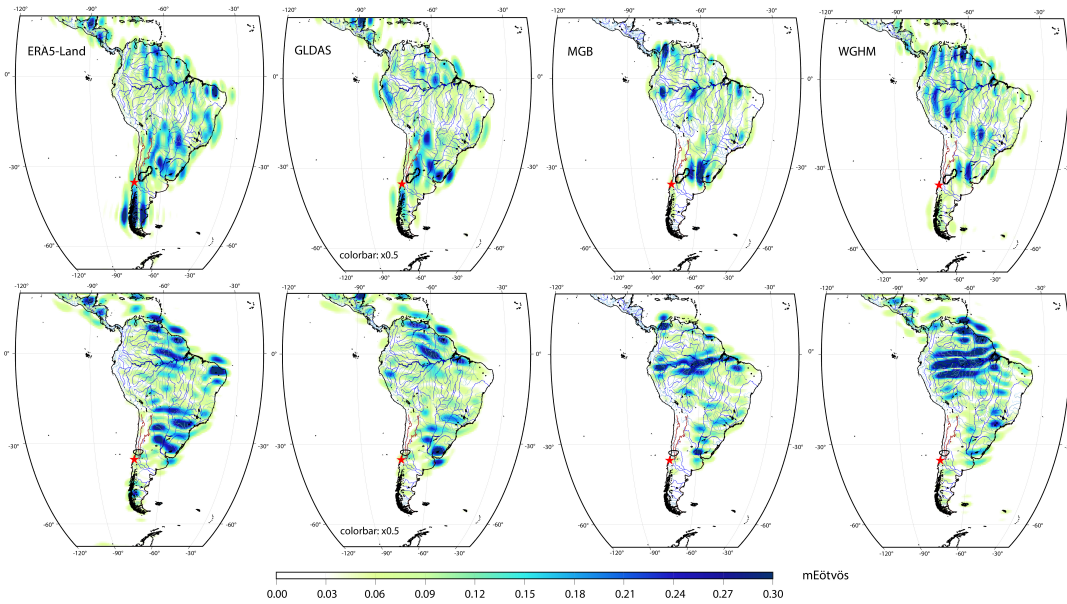


Figure S8: Spatial patterns of the non-seasonal signals in the gravity gradients from the ERA5-Land, GLDAS, MGB and WGHM hydrology models, as expressed by the rms of the 2009/09 – 2010/02 time series of gravity gradients at the scale 500-km (top line: $\phi\phi$ gradients in the local spherical frame, emphasizing North-South oriented signals; bottom line: $\theta\theta$ gradients, emphasizing East-West oriented signals). The annual, semi-annual and long-term trend components have been removed. Black lines, top panels: 0.15 mEötvös contour of the GRACE GRGS anomalous signal before the Maule earthquake shown in Main Fig. 3d. Black lines, bottom panels: 0.1 mEötvös contour of the GRACE GRGS East-West oriented anomalous signal in February 2010. Due to a high level of East-West elongated artefacts in the $\theta\theta$ gradients at the 500-km scale, it is approximated by the contour of the $\theta\theta$ gradients after a 30° clockwise rotation of the spherical frame.

895 **G.2 2003-2009 period**

896 Over the 2003-2009 period, in the 500-km scale gravity gradients, the modelled hydrologi-
897 cal signals remain very low (Fig. S9). In large basins as the Amazon and La Plata, this can
898 be due to a different characteristic scale of the signals (larger than 500-km). See Section
899 H.3 for a discussion of the ERA5 signal near the epicenter in the $\phi\phi$ gradients.

900

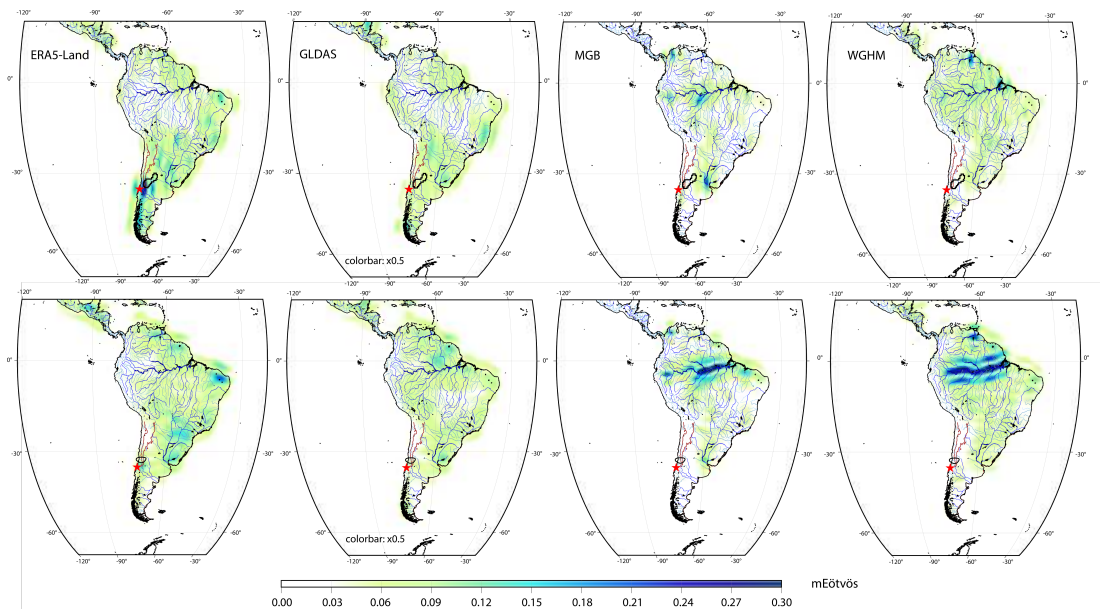


Figure S9: Same as Fig. S8, for the period 2003/01 – 2009/12.

901 **G.3 The seasonal cycle in ERA5-Land**

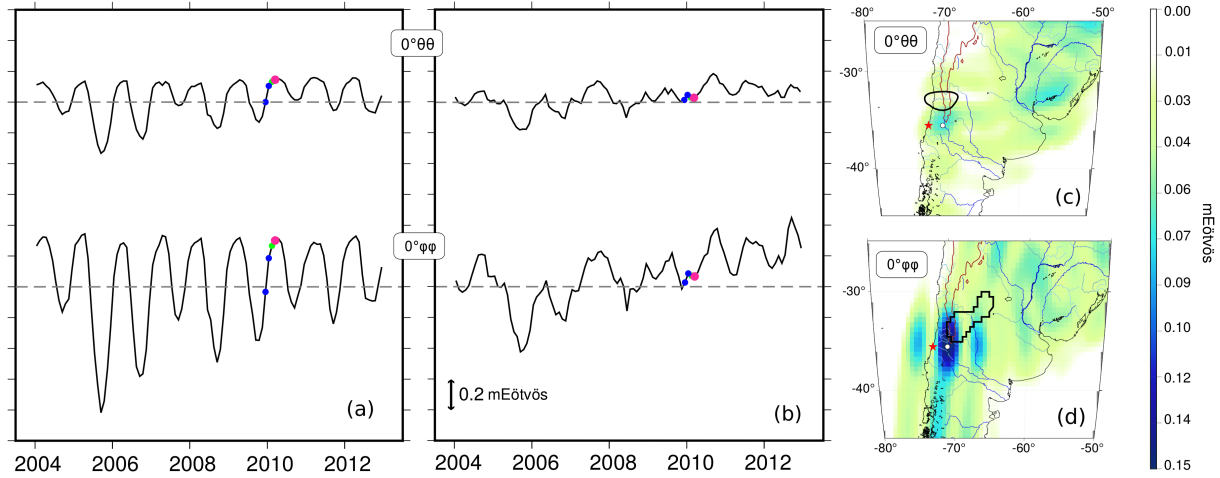


Figure S10: Time series and RMS maps over the 2003/01 – 2009/12 period, for the 500-km scale gravity gradients in the local spherical frame, computed from the ERA5-Land hydrological model. Panel a (resp. b): time series before (resp. after) correction for the annual and semi-annual cycles over the 2003/01 – 2008/12 period for the $\theta\theta$ (top) and $\phi\phi$ (bottom) gravity gradients. Panel c,d: RMS maps after correction for the annual and semi-annual cycles, for the $\theta\theta$ (panel c) and $\phi\phi$ (panel d) gravity gradients.

902 When comparing the hydrological models, we noticed differences between ERA5 and
 903 the other models. The ERA5 water storage amplitude appeared about twice larger than
 904 that of all the other models, hence the scaling by a factor of 0.5 applied for comparisons.
 905 In the Andean Cordillera close to the Maule region, contrary to the other hydrological
 906 models, the amplitude of its annual cycle varies irregularly by a factor up to 2.5 in the
 907 North-South gravity gradients, making the seasonal correction difficult (see Figure S10).
 908 This is why the RMS map of ERA5 in Fig. S8e comprises a small signal near Maule in
 909 the North-South direction (also present in the 2003-2009 period, see Appendix Fig. S9).
 910 Nevertheless, this contribution cannot explain the GRACE anomaly before the earthquake
 911 due to different spatial and temporal patterns. The geometry of this ERA5 signal indeed
 912 follows the topographic reliefs of the Andes, leading to an absence of signal in the East-
 913 West direction and at the larger 800-km scale in the North-South direction. In addition,
 914 its time evolution is roughly periodic.

915 **H Observed vs predicted anomalous February 2010 sig-**
 916 **nals over South America**

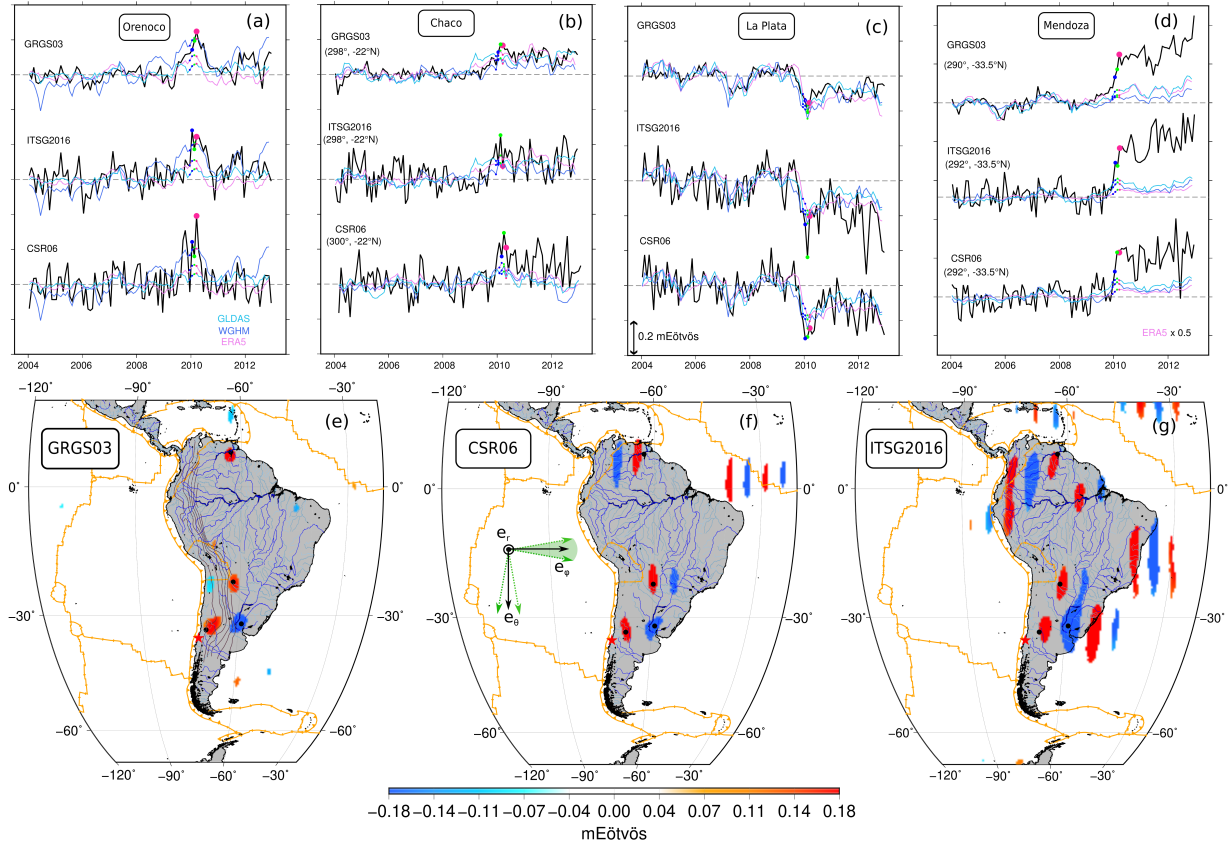


Figure S11: Anomalous signals in February 2010 in different GRACE solutions, without any hypothesis on a step-like evolution of the time series, compared with the predictions of hydrological models. Bottom panels e-g: maps of anomalous 800-km scale, $\phi\phi$ gravity gradients in the local south-east-up spherical frame, emphasizing North-South oriented signals, for each GRACE solutions in February 2010 (GRGS: panel e, CSR: panel f and ITSG-2016: panel g). The anomalous February 2010 signals shown in these maps are those outside the [1-99%] percentile range of the long-term residual time series $g(t)$ (see Section 2.4) for the CSR solution, outside the [2.5-97.5%] percentile range for the ITSG-2016 solution, and outside the [2.5 10^{-5} - 99.99975%] percentile range for the GRGS solution. Top panels a-d: time series of the GRACE gravity gradients (black) and the predicted gravity gradients from three hydrological models (colors) for the same scale and orientation as in the maps e-g. The time series are given at the locations of the signals common to the three GRACE solutions in February 2010: a) Orenoco river ($8^{\circ}N, 297^{\circ}E$), b) Pilcomayo river ($22^{\circ}S, 298^{\circ}E$), c) La Plata ($32^{\circ}S, 301^{\circ}E$) and d) Mendoza ($33.5^{\circ}S, 290^{\circ}E$). These locations are marked by black dots on the maps.

917 I Observed vs modelled co-seismic signal

Layer	Depth (km)	V_P (m.s ⁻¹)	V_S (m.s ⁻¹)	ρ (kg.m ³)
1	0 – 70	6700	3870	2900
2	70–	8000	4620	3400

Table 1: Earth model parameters for the modelling of the gravity gradient signals associated with the co-seismic rupture and the pre-seismic normal faulting.

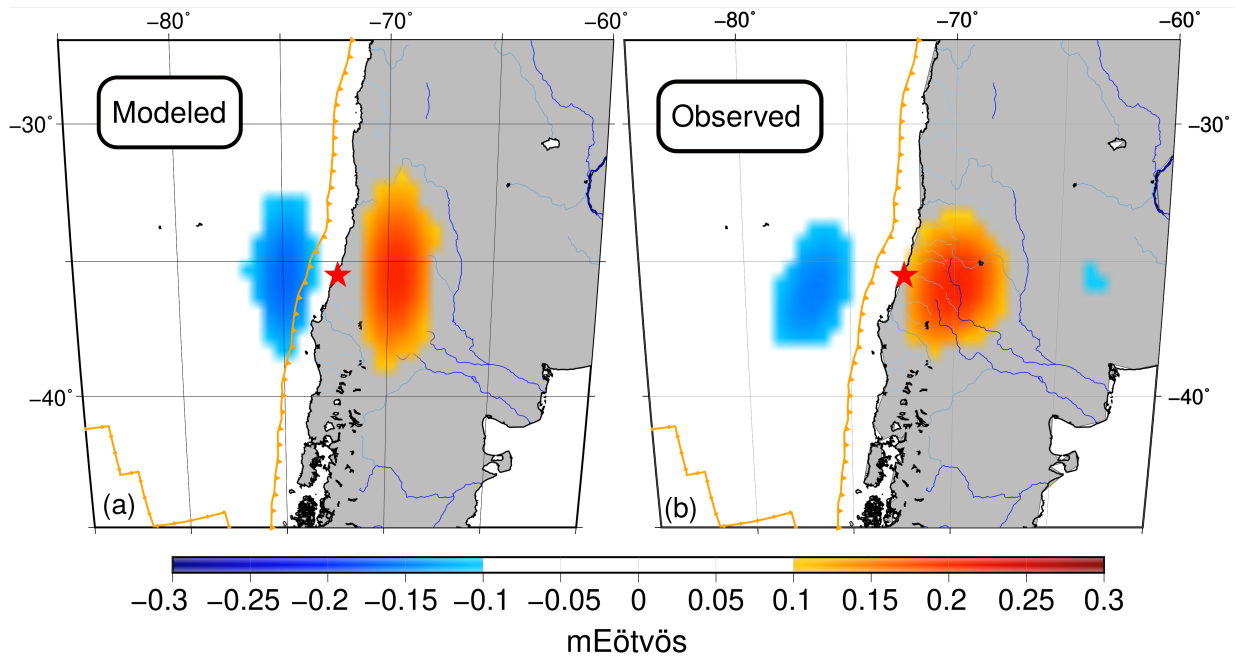


Figure S12: Comparison between the modeled and the GRACE-observed co-seismic gravity gradient signal (scale 800-km, $\phi\phi$ gravity gradients in the local south-east-up spherical frame). Panel a: gravity gradient signal predicted from the co-seismic slip model by [27] (based on the spherical harmonics expansion of the corresponding geoid signal up to degree/order 60). Panel b: co-seismic step estimated in the GRACE GRGS gravity gradients in March 2010 (same as Main Fig. 1d)